Development of hybrid nanomaterials based on MXene/Fe_3O_4 magnetic nanoparticles for photo-magnetic hyperthermia applications

Zhu Peng Shen [a], Juan Carlos Cabanelas [a], Álvaro Gallo-Cordova [b], Lucía Gutiérrez [c], Yílian Fernández-Afonso [c], Verónica S Miguel[a], Julio Marco Cuenca [e], Ángel Maroto-Valiente [d], Helena Gavilán [e,*], María B Serrano [a,**].

[a] Department of Materials Science and Engineering, IAAB. Universidad Carlos III de Madrid, Leganés, Madrid, 28911, Spain

[b] Department of Nanoscience and Nanotechnology, Instituto de Ciencia de Materiales de Madrid (ICMM-CSIC), Madrid, Madrid, 28049, Spain

[c] Instituto de Nanociencia y Materiales de Aragón (INMA) CSIC-Universidad de Zaragoza, Zaragoza, 50018, Spain

[d] Dpto. Química Inorgánica y Química Técnica, Facultad de Ciencias, UNED, 28232 Las Rozas de Madrid, Madrid, Spain

[e] Department of Physical Chemistry, Universidad Complutense de Madrid, Madrid, 28040, Spain

*** Corresponding author. Department of Physical Chemistry, Universidad Complutense de Madrid, Madrid, Madrid, 28040, Spain. E-mail:** hgavilan@ucm.es

**** Corresponding author. Department of Materials Science and Engineering, Universidad Carlos III de Madrid, Leganés, Madrid, 28911, Spain. E-mail:** berna@ing.uc3m.es

Abstract

MXenes are two-dimensional transition metal carbides that have emerged as versatile nanomaterials. Their distinctive physicochemical properties and surface characteristics

make them ideal platforms for engineering hybrid nanomaterials. The combination of MXenes and magnetic nanoparticles (MNPs) into a single nano-object leads to materials with interesting properties (ferrimagnetism, mechanical strength, and conductivity, etc.) for a broad range of applications. MXenes exhibit good compatibility and excellent photothermal (PTT) properties; while MNPs, particularly iron oxide nanoparticles (IONPs), are exploited for biomedical applications through magnetic hyperthermia (MHT). This work focuses on the development of hybrid nanomaterials combining MXenes and IONPs, prepared through a simple, holistic, and reproducible method. The surface of delaminated MXenes (dMXenes) sheets was covered with well-defined shape IONPs of 14 nm. We have used faceted nanoparticles, to achieve point-of-reference magnetic hyperthermia performance. The surface loading of IONPs on the MXenes was controlled by varying the MXene-to-MNPs mass ratio from 10:90 to 90:10The potential of the hybrids for photo-magnetic hyperthermia was evaluated using near-infrared (NIR) light (1064 nm, 1 W) and alternating magnetic fields (AMFs) of 9.5–17.0 kA/m and 282 kHz, determining their specific absorption rates (SAR) values. While for MHT, SAR values are up to 150 W/g (Fe_3O_4) for 50:50 hybrid, the characterization of this new nanomaterial revealed a synergistic behavior in PTT, achieving SAR values up to 577 and 1106 W/g (hybrid), for 50:50 and 70:30 mass ratio hybrids, respectively. This work demonstrates the heat dissipation capability of MXene/IONPs hybrids under AMFs and via laser excitation.

Keywords

MXenes, Ti_3C_2Tx, magnetic nanoparticles, IONPs, hybrid nanoparticles, photothermia, magnetic hyperthermia

1. Introduction

The therapeutic modalities of magnetic hyperthermia (MHT) [1] and photothermal therapy (PTT) [2,3] are nano-therapies based on the elimination of cancer cells through heat generation upon exposure of tumor cells to either alternating magnetic fields (AMF) or light (near-infrared radiation (NIR)). MHT relies on the use of magnetic nanoparticles (MNPs) such us superparamagnetic iron oxide nanoparticles (IONPs) [4,5] (*e.g.*, magnetite — Fe_3O_4 or maghemite — γ-Fe_2O_3), which act as a transducers, converting electromagnetic energy into heat upon exposure to an AMF in the kHz radiofrequency range (100–300 kHz) and a specific field intensity (few tens of kA/m) [6]. For a safe MHT treatment, AMF conditions (amplitude and frequency) must remain below certain limits [7]. In contrast, PTT relies on the use of agents that absorb light energy (via laser excitation of at appropriate wavelength), leading to electron excitation and subsequent non-radiative relaxation, which results in heat release [8]. As NIR penetrates deeper into the human body than visible light, it is generally preferred for any biomedical applications designed. From the different windows that can be identified in the NIR (first, second and third biological windows), the second (NIR II, with λ between 1000 nm and 1350 nm) presents a maximum optical penetration depth in the skin [9,10]. For this reason, PTT agents are typically excited using a laser with a wavelength of 1064 nm. Currently, these nano-therapies are used as adjuvant treatments to inhibit local recurrence of the tumor [11] and in the earlier stages of anticancer treatments along with chemotherapy or radiotherapy [12].

Although both MHT and PTT are considered non-invasive thermotherapies, recent research has increasingly focused on developing novel agents with greater efficiency, performance, and selectivity [13]. Concerning MHT, MNPs have been specifically designed and optimized for this application in terms of their size and size distribution

[14], crystallinity [15], shape, composition, magnetic parameters and their aggregation/assemblies state [7]. It is worth noting that, despite the variety of nanomaterials reported, MHT in clinical trials conducted in Europe and in the US has centrally relied on the use of IONPs [16]. In the case of NIR-PTT, various agents have demonstrated promising photothermal properties, including plasmonic nanoparticles, (*e.g.*, Au) [17], carbon-based materials (*e.g.*, graphene, carbon nanotubes and carbon dots) [18], and organic dyes (*e.g.*, cyanines) [19]. More recently, 2D transition metal dichalcogenides [20,21] have demonstrated to exhibit significant advantages for photo/thermo-based tumor therapies compared to traditional nanomaterials, owing to their high specific surface area, excellent biocompatibility, and strong NIR photothermal absorption. For example, nanosheets of MoS_2, WS_2, TiS_2, and Bi_2Se_3 have been employed as photothermal agents for cancer treatment, exhibiting high light-to-heat conversion efficiency [22]. Moreover, because of their large surface area, these atomic-thin nanosheets have also been explored as nanoparticle carrier platforms for the development of multifunctional heterostructures in combined photothermal therapies [23,24].

In addition, several studies have highlighted that high thermal conductivity is crucial for efficient heat distribution, as it ensures uniform thermal transfer across the material while minimizing energy losses [25]. Carbon-based materials, which are effective photon captors, exhibit excellent photothermal efficiency, high thermal conductivity, and large aspect ratio, making them ideal candidates for advanced photothermal applications. However, these materials present certain limitations, such as poor dispersibility in various solvents, which can hinder their practical application. On the other hand, plasmonic nanoparticles such as silver, gold, and aluminum, have shown significant potential as PTT agents [26]. Their tunable optical properties, controlled by size, shape, and composition, enable precise adjustment for specific therapeutic needs. Furthermore, plasmonic

nanoparticles are chemically stable and can be functionalized with biomolecules, enhancing their biocompatibility and enabling targeted therapy. However, their practical application is limited by narrow absorption bandwidths and their toxicity is questioned at high concentrations, which could restrict their safe use in clinical settings. To overcome the limitations, nanomaterials with larger aspect ratios and enhanced biocompatibility offer a promising alternative, enabling more efficient and uniform heat distribution even at low concentrations. MXenes emerge as highly promising phototherapeutic agents due to their exceptional metallic conductivity, excellent biocompatibility, and photodynamic properties, making them particularly suitable for applications such as cancer treatment [27].

$Ti_3C_2T_x$-type are the first MXenes and the ones with the most applications currently used. Because of their high electronic conductivity and versatile chemistry surface, they have shown a variety of applications, including energy storage, electromagnetic interference (EMI) shielding, gas and pressure sensors, water purification, photo- and electrocatalysis, and photothermal agent, among others [27]. In the biomedical field, their notable application is as a photothermal agent for eliminating cancer cells. This is due to the nanomaterial's ability to absorb electromagnetic radiation in the NIR I and II biological windows [28]. Specifically, in NIR II, there is significant interest as these wavelengths achieve improved tissue penetration without causing damage from self-heating or tissue contraction [29]. Additionally, the $Ti_3C_2T_x$-nanolayers exhibit a 100% light-to-heat conversion rate [30], attributed to their quasi-metallic nature and the strong effect of plasmonic surface resonance (SPR) [31]. Combined with plasmonic nanoparticles, they can exhibit plasmonic effects like metallic nanostructures when exposed to NIR light, leading to the enhancement of light-matter interaction, with enhanced absorption and high photothermal conversion efficiencies [32]. A notable

example is the work of Fan *et al.* [33] who developed a new hybrid nanomaterial combining plasmonic silver nanoparticles (AgNPs) and 2D MXene nanosheet enabling effective photothermal conversion. These nanomaterials were employed as photothermal fillers within a transparent, wearable polyurethane device, which exhibited outstanding photothermal conversion efficiency, high thermal conductivity, and light-triggered healing properties.

In this work we focus on the fabrication of hybrid nanomaterials combining MXenes and magnetic IONPs. $Ti_3C_2T_x$-type MXenes, besides having high light capture in NIR II range, offer advantages over other nanomaterials such as adjustable optical properties by changing the number of layers or through a superficial modification [34–36]. On the other hand, IONPs have been selected as part of the composite given their low cytotoxicity, high biocompatibility [37] and appealing magnetic properties, including their high efficiency for MHT, and their ability to be guided to and concentrated in tumors using magnetic field gradients, further leading to drug-delivery systems. Moreover, IONPs can be traced *in vivo* through various imaging techniques, including magnetic resonance imaging (MRI), magnetic particle imaging (MPI), magneto-acoustic imaging and photo-acoustic imaging [38].

IONPs used in this work were synthesized via a high temperature thermal decomposition method, enabling precise control over their size and shape, using benzaldehyde as shape-directing agent and oleic acid as hydrophobic ligand, [39]. During the current research hydrophilic $Ti_3C_2T_x$-type MXenes, were synthesized by selectively etching aluminum from their parent MAX phase (Ti_3AlC_2) employing a mixture of LiF and HCl solution, following a synthesis protocol similar to that reported by Gogotsy *et al.* [40]. The deposition of IONPs onto delaminate MXenes was conducted through a simple and reproducible van der Waals-facilitated self-assembly method, coupling the

nanoparticles and MXenes as reported by Zhang *et al.* [41]. We produced hybrids systematically varying the MXene:IONPs mass ratio and obtaining hybrids of MXenes with different IONPs coverage. IONPs concentration was found to be a key parameter that affects the number of MXene sheets stacked while forming the hybrid in a colloidal dispersion. Finally, we evaluated their properties as photo- and/or magnetothermal agents by determining the specific absorption rates (SAR) values when subjecting aqueous dispersions of the hybrids to AMFs of different field amplitudes (9, 13 and 17 kA/m) and a frequency of 282 kHz; and to NIR radiation in the second biological window using a laser with λ = 1064 nm and 1 W of power. MXene:IONPs mass ratios of 50:50 and 70:30 were found to lead to hybrids with the best magnetic-field-to-heat and light-to-heat conversions.

This study presents the first comprehensive evaluation of this type of hybrid nanomaterials (MXenes and IONPs) for dual-mode magnetic hyperthermia and photothermia, offering a thorough magnetic characterization and hyperthermia responses under different stimuli, *e.g.*, AMFs and laser irradiation. The AMFs and laser parameters here employed are safe for the clinic (1 W for the photothermal characterization and 9-17 kA/m at 282 kHz for magnetic hyperthermia evaluation). Unlike previous studies, we explore the synergistic potential of hybrid nanomaterials to achieve enhanced and controllable thermal effects. By characterizing the hyperthermal response of different hybrid nanomaterials whose MXene:IONPs mass ratio has been varied, we demonstrate improved heating efficiency, greater tunability, and certain nanomaterials have potential for optimized cancer therapy. This novel insight paves the way for multifunctional nanoplatforms, expanding the scope of nanomedicine.

2. Results and discussion

2.1. Delaminated $Ti_3C_2T_x$-type MXene (dMXene) characterization

The morphology of the dMXenes was studied by scanning electron microscopy (SEM). Using secondary electron mode (**Fig. 1a** and **1b**), it was possible to identify micro-sized (>10 μm in length) sheets with completely smooth surfaces and showing a delaminated structure with a very high aspect ratio. Thickness estimation of the Ti_3C_2 sheets was not straightforward from the SEM images, but the reported values in the literature for single-layers are in the range of 1.14–1.18 nm [42]. With the backscattered electron mode (**Fig. 1c** and **1d**) it was possible to determine the absence of contaminants and TiO_2 oxide clusters, which would appear upon MXene oxidation as bright spots over the sheets [43]. Controlling the size and thickness of MXene nanosheets has been reported to be critical for PTT and its optimization depends on the intended application. For example, Perini *et al*. reported that the fewer MXene sheets stacked for thin films of MXenes, the higher the thermal conversion [44]. It is also known that high thickness in $Ti_3C_2T_x$-type MXenes limits their applicability in biomedicine [45]. In addition, it is reported that few layer $Ti_3C_2T_x$ MXenes show good biocompatibility [46].

The crystalline structure of MXene was analyzed by X-ray diffraction (XRD). The diffractogram obtained is presented in **Fig. 1e**, showing a high intensity signal located at 5.98° belonging to the plane (002) of $Ti_3C_2T_x$ and a lower intensity signal at 17.85°, which is the consecutive plane (004). The position of these planes (2θ) is a product of the stratified structure composed of different overlapping layers; therefore, the values change inversely proportional to the interplanar distance [47]. It is well known that when $Ti_3C_2T_x$ sheets are stacked, broad and poorly defined signals appear in the range between 30 and 70°, while when they are delaminated the diffractogram becomes more ordered, with very well defined (00*l*) signals. If a severe delamination is obtained, the relative intensity of

the (002) signal increases with respect to the other (00*l*) signals [48,49], and this is the case of the synthesized MXenes, as shown in **Fig. 1e**.

Applying Bragg's law on the strongest signal, the value of *d*(002)-spacing was determined to be 14.8 Å. This distance accounts for the thickness of a single Ti_3C_2 sheet, including its T_x terminations and intercalating species, such as H_2O molecules or other components that prevent the sheet staking. Additionally, knowing that the Ti_3C_2 crystallizes in a hexagonal system with a *P6₃/mmc* space group [50], the *c*(002)-lattice parameter was calculated to be, 29.6 Å. This parameter represents the lateral distance between two consecutive monolayers, including their respective intercalating species, as shown in the inset of **Fig. 1e**. Based on the values of both parameters, the presence of intercalating water molecules or Li^+ cations, originating from the LiCl salts generated during the synthesis, can be inferred [49].

XRD can also be used to assess whether the MXenes have undergone oxidation, indicated by characteristics TiO_2 diffraction peaks, or if the aluminum etching process was incomplete. In both cases, additional diffraction peaks would appear between 25 and 45° [51]. It can be assumed that the analyzed dMXenes are of few-layered, based on the low intensity of the (004) plane, and of high purity, as indicated by the absence of TiO_2 oxides or unreacted MAX phase, consistent with SEM images.

Fig. 1f presents the XPS survey spectrum of the MXene nanosheets (red line in the figure), showing the typical peaks for Ti 2p, C 1s, O 1s and F 1s, and total absence of Al 2p or Al 2s peaks (which should appear at around 74 and 116 eV, respectively) confirming the satisfactory etching of the aluminum layer. XPS also confirms the presence of T_x (-F/-O/-OH) surface termination groups because of the synthesis procedure. High resolution spectrum for Ti 2p is shown in **Fig 2b**, while the high-resolution spectrum for C 1s, O 1s and F 1s regions are presented in supplementary **Fig S1.** The C 1s spectrum

shows an intense C-Ti peak centered at 282 eV belonging to the dMXene structure. F 1s and O 1s peaks belong mainly to T_x (C-Ti-F and C-Ti-O) surface terminations. We have carefully performed the curve fitting of the Ti 2p XPS region according to bibliography [52] to characterize the oxidation state and surface condition of the dMXene sheets. The quantification of Ti 2p peaks is typically performed by considering either the different oxidation states of Ti (i.e. Ti^{+} Ti^{2+}, etc.) or the local environment of Ti atoms (C from the MXene structure or O and/or F atoms from T_x terminations) depending on their network position. We have not delved into this aspect as it is tangential to the scope of this work. Consequently, peak fitting was conducted following standard procedures widely supported in the academic literature [53], and it is presented in **Fig. 2b**. The deconvoluted spectra of Ti 2p was adjusted to three doublets (Ti $2p_{3/2}$ and Ti $2p_{1/2}$) centered at 455.0/460.9, 455.9/461.7, and 457.2/462.4 eV, which are ascribed to C-Ti-C, C-Ti-O and C-Ti-F, respectively. The relatively high fraction of the last doublet (29%) indicates a significant fluorine content, attributed to the high concentration of HF generated in situ during synthesis. Additionally, a fourth doublet centered at 459.2/463.8 eV was required for proper fitting, which we assigned to $TiO_{2-x}F_{2x}$ oxide species [52]. This doublet likely originates from the partial oxidation of MXenes during synthesis and delamination. The fraction of this doublet is nevertheless low, supporting the XRD and SEM findings, which indicate that the dMXene sheets are stable and largely non-oxidized.

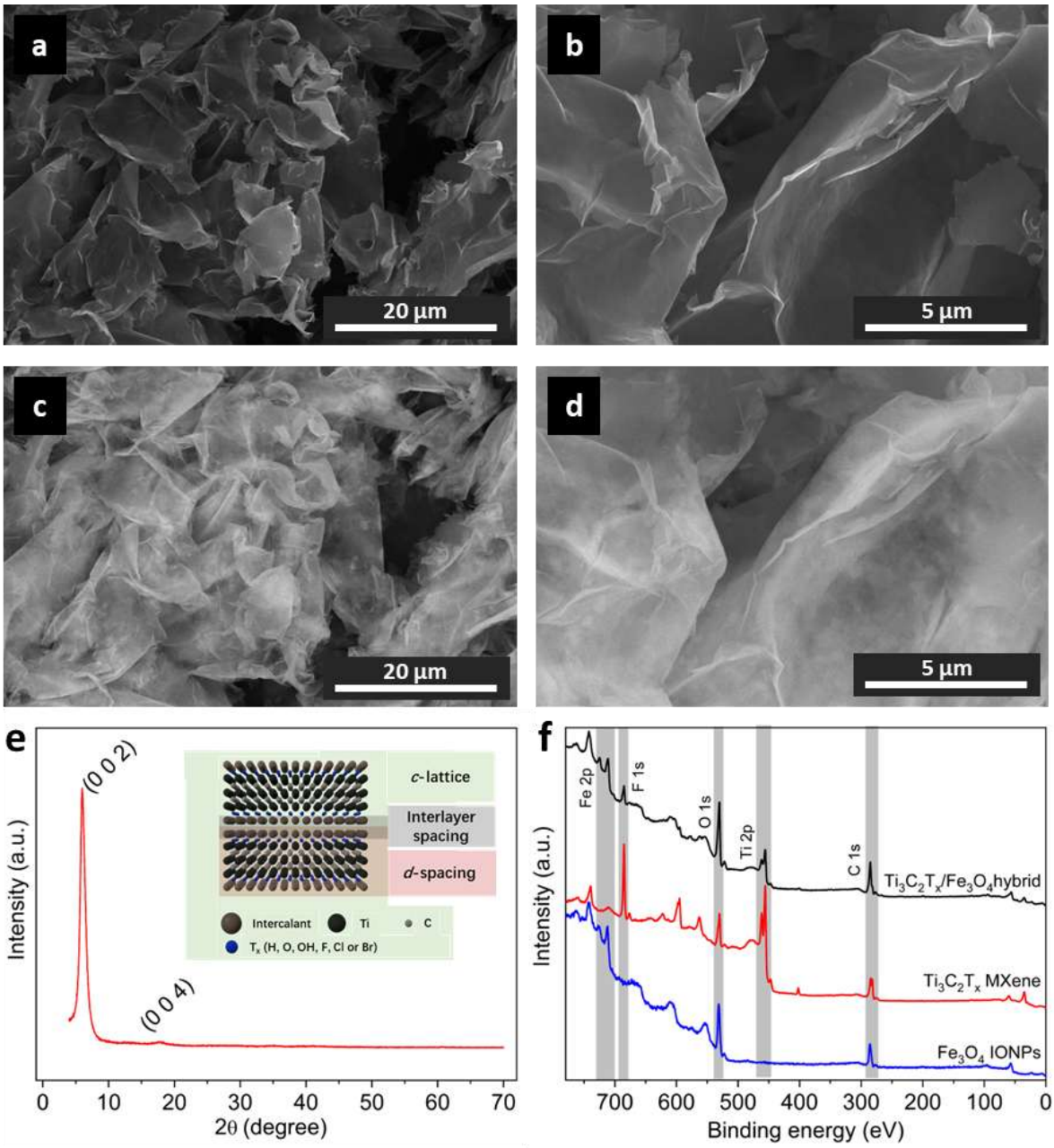

Fig. 1. (a–d) SEM micrographs at different magnifications: (a and c) ×2000 and, (b and d) ×8000 of few layer $Ti_3C_2T_x$ nanosheets registered by (a and b) secondary electrons mode and (c and d) backscattered electron mode. (e) Diffractogram of delaminated $Ti_3C_2T_x$-type MXene nanosheets. Insert shows the atomic structure of a $Ti_3C_2T_x$ bilayer with intercalants. (f) XPS Survey spectrum of $Ti_3C_2T_x$ dMXene nanosheets, Fe_3O_4 IONPs, and the representative 50:50 $Ti_3C_2T_x/Fe_3O_4$ hybrid material.

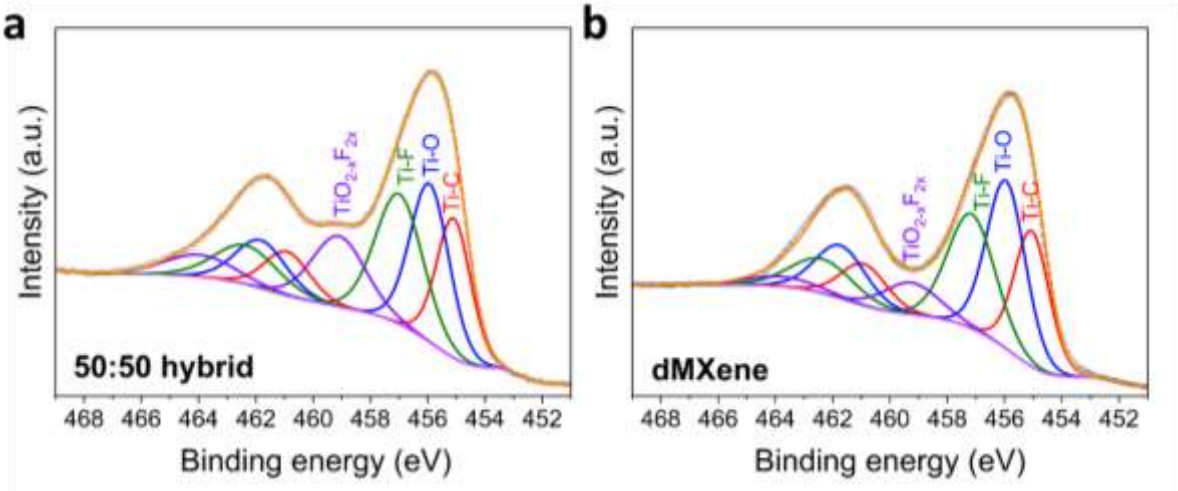

Fig. 2. High resolution XPS profiles for Ti 2p region: (a) 50:50 hybrid (b) dMXene sheets.

2.2. Fe_3O_4 IONPs characterization.

Fe_3O_4 IONPs were obtained according to a previous reported protocol reported by Qiao *et al.* [54], based on the thermal decomposition of $Fe(acac)_3$ in 1-octadecene at high temperature (280 °C) in the presence of different additives and ligands, including TDD, OAm, OA and BA (see experimental section). This reaction comprises 2 steps: first, all the reagents are dissolved, and the reaction mixture is degassed under a nitrogen flux (110 °C), and second, the temperature is raised until reflux (280 °C). Representative TEM images of the synthesized materials are shown in **Fig. 3**. IONPs show quasi-cubic faceted faces. Size distribution and shape can be controlled by the relative amount of the synthesis additives and ligand. Aromatic aldehydes, like benzaldehyde, promote cubic ferrite nanoparticles, while aliphatic aldehydes yield spherical ones [55].

The size of IONPs is centered at 14 nm. Corresponding size distribution is shown in **Fig. 3c**, revealing it is monomodal and with low polydispersity (polydispersity index PDI<<0.1). The size distribution fit well to a Lognormal distribution function. TEM images show interparticle distance around 1.5–2.0 nm attributed to the presence of oleic

acid. XPS survey spectrum of synthesized IONPs is presented in **Fig. 1f**. The characteristic doublet peaks of Fe $2p_{3/2}$ and Fe $2p_{1/2}$ are clearly observed at around 712 eV and 725 eV respectively, as well as Fe, C and O peaks. High resolution spectra of Fe, C and O regions are presented in supplementary material (**Fig. S1**). The high intensity of the C 1s peak confirms the presence of oleic acid coating the surface of the IONPs.

The stability of the IONPs was evaluated in tetrahydrofuran (THF), which is the solvent used to form the $Ti_3C_2T_x$/IONPs hybrids. For this purpose, IONPs initially dispersed in chloroform were subsequently transferred to THF. Nanoparticles dispersion diluted at a 1:40 volume ratio in THF were analyzed using dynamic light scattering (DLS). The size distributions by number, and volume for IONPs are shown in **Fig. S2** with results summarized in **Table S1**. The hydrodynamic size of the IONPs (Z-average values) is around 100 nm with PDI index of 0.37. Indeed, Number-weighted data (17 ± 3 nm) agrees with particle size determined by TEM. Volume and Intensity-weighted data confirms the presence of secondary peaks of lower intensity at 400 nm and above, which may be associated with the presence of clusters of IONPs. Despite the presence of secondary peaks (reflecting the presence of some clusters of IONPs), Z-average values confirm that the dispersions of IONPs are stable in THF, the medium used for hybrid preparation. As such, we expect that both single nanoparticles and clusters of IONPs interact with MXenes to form heterostructures.

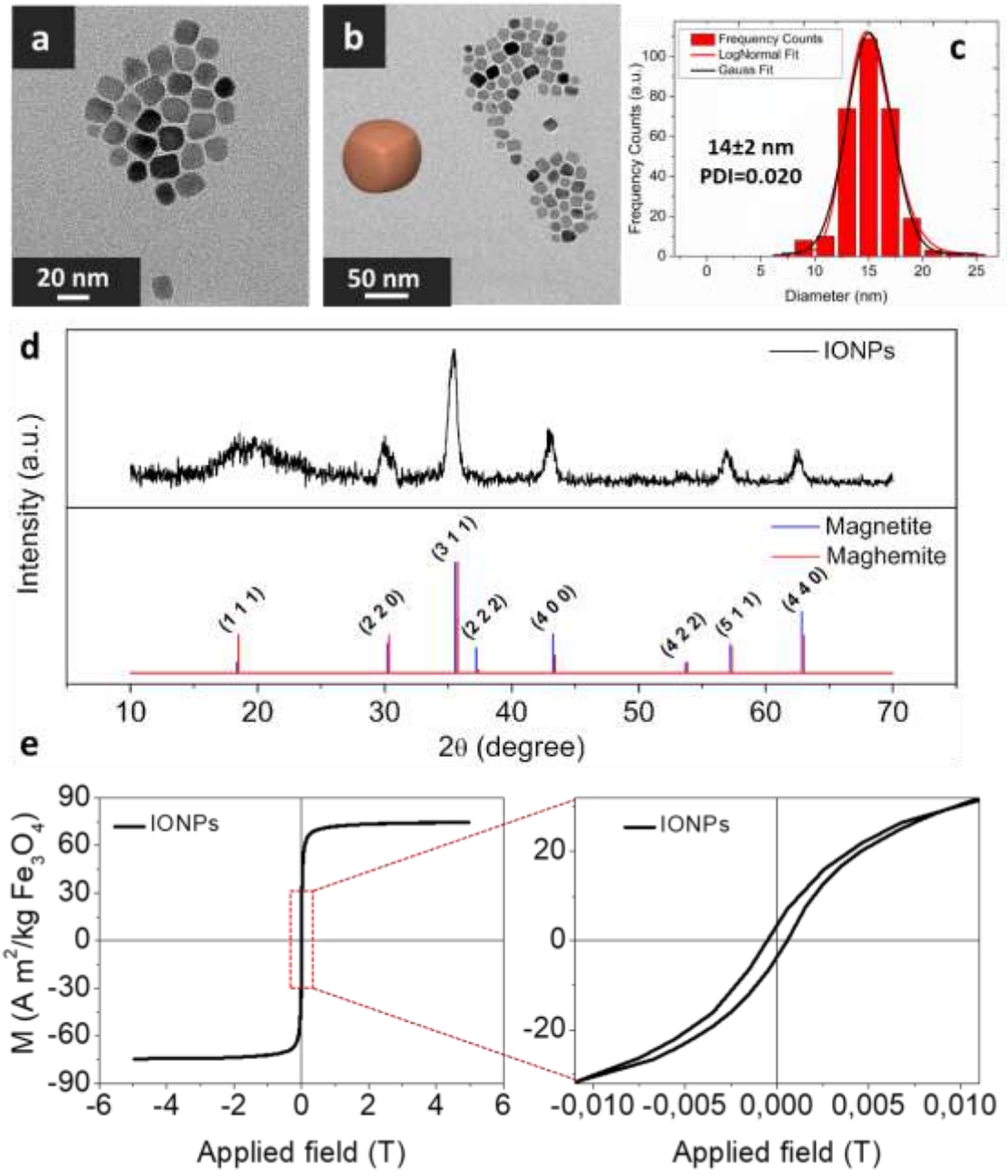

Fig. 3. (a and b) TEM micrographs at different magnifications (×60000 and ×200000) of IONPs; (c) size distribution. (d) Diffractograms of IONPs with indexed magnetite and maghemite patterns. (e) Hysteresis curves of IONPs at different scales.

Table 1. Summary of magnetic nanoparticles characterization parameters (PDI: polydispersity index, M_S: magnetic saturation, M_R: magnetic remanence, H_C: coercivity).

Technique	**Parameter**	**Value**
TEM	Morphology	Faceted
	Size (nm)	14 ± 2
	PDI	0.020
DLS	PDI	0.38
XRD	*a*-lattice (Å)	8.38
VSM	M_S (A m^2/kg)	74.5
	M_R (A m^2/kg)	3.34
	H_C (T)	5.67×10^{-4}

The XRD diffractogram of IONPs is presented in **Fig. 3d** along with the reference diffraction patterns of iron oxides, including magnetite (Fe_3O_4) with an inverse spinel structure and its low-temperature oxidized phase, maghemite (γ-Fe_2O_3) [56].

Indeed, the peaks are attributed to the presence of iron oxide. XRD confirms the high crystallinity of the IONPs. The *a*-lattice parameters were determined by applying Bragg's law to the highest intensity peak in the (311) plane. The results are shown in **Table 1**.

The key characteristic of magnetite (Fe_3O_4) is its 2:1 Fe^{3+}/Fe^{2+} ratio, giving a lattice spacing of 8.39 Å, slightly larger than the 8.33 Å of maghemite (γ–Fe_2O_3), which contains only Fe^{3+}. This lattice spacing difference confirms that the nanoparticles are predominantly magnetite [57]. Thus, XRD analysis suggests (*a*-lattice 8.38 Å) that the nanoparticles primarily comprise magnetite.

The magnetic behaviour of the synthesized nanoparticles was studied using DC magnetometry and a Vibrating Sample Magnetometer (VSM). Field-dependent magnetization curves of the MNPs registered at room temperature are shown in **Fig. 3e**. IONPs show a high saturation value (74 A m^2/kg Fe_3O_4) attributed to the faceted morphology, which grants lower surface spin disorder and thus higher M_S [58]. This value is slightly lower to the values reported for bulk magnetite at room temperature (92 A m^2/kg Fe_3O_4) [59]. Toyos-Rodríguez C. *et al.* [59] obtained similar values of M_S (70 A m^2/kg Fe_3O_4) for 15 nm Fe_3O_4 magnetic nanoparticles. As for M_R and H_C, shown in **Table 1**, they are negligible; thus, the IONPs have essentially superparamagnetic behavior.

2.3. $Ti_3C_2T_x$/Fe_3O_4 nanohybrids characterization

Fig. 4a-f shows SEM micrographs of nanohybrids at different $Ti_3C_2T_x$/Fe_3O_4 weight ratios. A correlation between weight ratio and surface structure is observed. In the 90:10 hybrid, IONPs deposited on the surface of the MXenes are barely observed, and surface coverage is low. For the 70:30 hybrid, more IONPs are observed over the surface of the sheet, while in the 50:50 hybrid a surface saturation was reached in which almost the entire active surface of the MXenes was covered with IONPs. In both cases, the 2D laminar structure of MXene is preserved. However, as the concentration of the nanoparticles increases, surface agglomerates of IONPs appear, so these nanoparticles may be considered in excess respect to the available space on the surfaces of the MXene sheets. Hybrids 30:70 and 10:90 clearly exhibit agglomerates of IONPs, along with a noticeable loss of the structural arrangement of the MXene sheets. Notably, above the 50:50 ratio, the characteristic lamellar structure of MXene is compromised due to high concentration of IONPs, which accumulate and fill the cavities, causing the layers to stick

together. Representative TEM images are presented in **Fig 5b-e**, confirming the presence of agglomerates of IONPs for 30:70 and 10:90 hybrids.

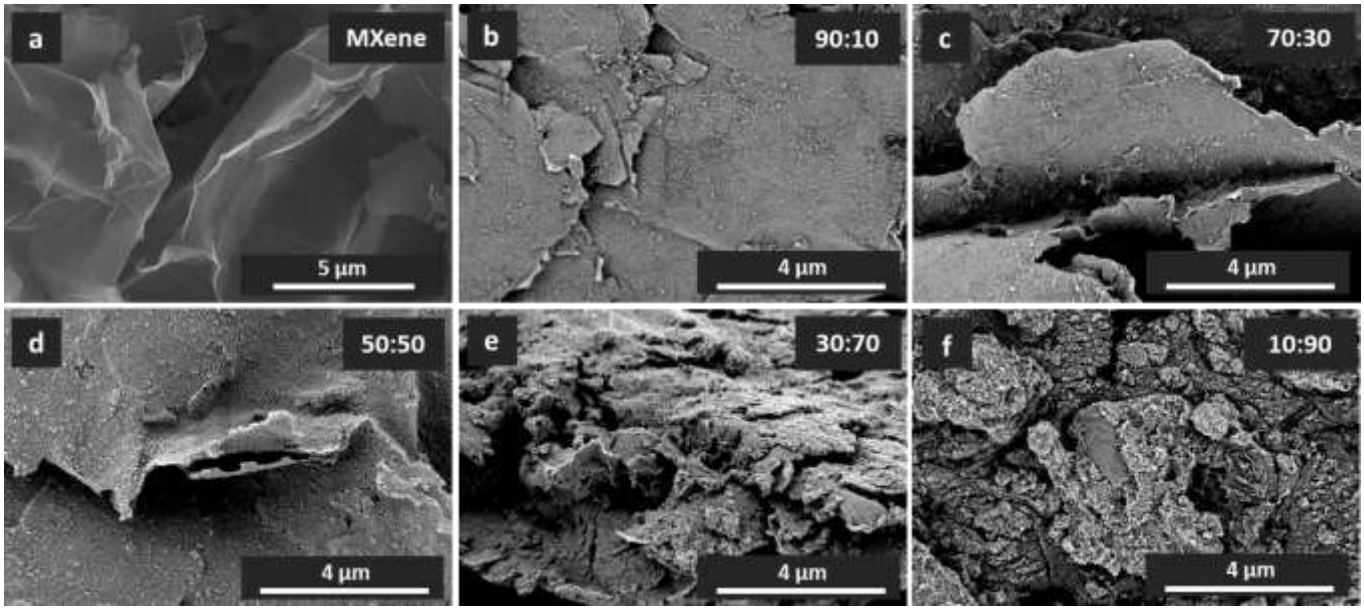

Fig. 4. SEM micrographs of (a) delaminated $Ti_3C_2T_x$-type MXene at ×8000 magnification captured using secondary electrons detector, and $Ti_3C_2T_x/Fe_3O_4$ hybrids with different mass ratios (b) 90:10, (c) 70:30, (d) 50:50, (e) 30:70 and (f) 10:90 captured with backscattered detector at ×12000 magnification.

The XPS survey spectrum of the $Ti_3C_2T_x/Fe_3O_4$ 50:50 hybrid is presented in **Fig. 1f** providing a comparison with the spectra obtained for dMXene nanosheets and IONPs. The hybrid spectrum exhibits a combination of characteristic peaks from MXene (Ti 2p, C 1s, O 1s and F 1s) and IONPs (Fe 2p, along with contributions from C 1s and O 1s), confirming the successful integration of both components in the hybrid structure. High resolution spectra for Fe 2p, C 1s, O 1s and F 1s are presented in supplementary **Fig. S1**. The C-Ti peak in the C 1s spectrum at 282 eV is diminished due to the contribution of C-C/C-O bonds from the oleic acid coating on magnetic nanoparticles. High resolution spectrum for Ti 2p region is shown separately in **Fig. 2a** and compared with the same region of dMXene nanosheets. A brief inspection of **Fig. 2** shows a significative

increment in the Ti region of the contribution of oxidized Ti species. Curve fitting of the Ti 2p XPS region for the hybrid was performed using the same procedure and conditions applied to the Ti 2p region of the dMXene sheets. Ti 2p region curve was again fitted to three doublets (Ti $2p_{3/2}$ and Ti $2p_{1/2}$) centered at 455.1/460.9, 455.9/461.8, and 457.0/462.3 eV, corresponding to C-Ti-C, C-Ti-O and C-Ti-F respectively; and a fourth doublet centered at 459.1/463.9 eV attributed to $TiO_{2-x}F_{2x}$ oxide species. The fraction of this doublet is noticeably increased compared to the bare dMXene, although its contribution remains below 20%. This suggests that the extended sonication process used in the holistic method for nanohybrids formation induces partial oxidation of the dMXene sheets. However, this oxidation does not significantly affect the laminar structure of the MXene or its ability to couple effectively with the IONPs, preserving the integrity of the hybrid material.

According to bibliography, specific surface area (SSA) of delaminated $Ti_3C_2T_x$-type MXenes may be considered around 12–20 m^2/g [25,60–62]. Specific surface area will be significantly influenced by the MXene surface nature, presence of intercalants and method of reparation. In fact, the accessible surface will be strongly influenced by the restacking of the MXene sheets, which is favored by the THF medium in which the hybrids were prepared. According to the SSA of MXene an ideal monolayer coverage of the entire surface by IONPs (considering them quasi-spherical and hexagonal package and a size around 15 nm) would be reached at around 0.75–1.25 g IONPs per g MXene. That is to say, for hybrids containing 44–56% by weight of MXene. Given the resulting 50:50 hybrid morphology (**Fig. 4d**), we surmise that nanoparticles such as magnetic Fe_3O_4 are able to act as intercalants between MXene layers [63,64], avoiding restacking in THF medium (see sketch in **Fig. 5a**). This has been confirmed through TEM analysis, which reveals distinct stacking arrangements for each hybrid mass ratio (**Fig. 5b-f**). This

phenomenon occurs during the hybrid fabrication process, where the continuous motion induced by sonication leads to variations in the interaction and assembly of MXene sheets and nanoparticles depending on their relative proportions. When the concentration of IONPs is low, as in the case of 90:10, the MXene sheets are able to form stacks. However, when the concentration increases, the IONPs act as intercalants, occupying interlaminar positions and preventing the formation of stacks, thereby maintaining separation between the lamellae. In extreme cases, such as the 10:90 hybrid, MXenes are delaminated, but the typical lamellar structure of the MXenes is disrupted, leading to the formation of large agglomerations of IONPs that can compromise the stability of the hybrid dispersion. Based on these results, hybrids with MXene:IONPs ratios of 70:30, 50:50 and 30:70 were selected for photothermal and magnetothermal evaluations.

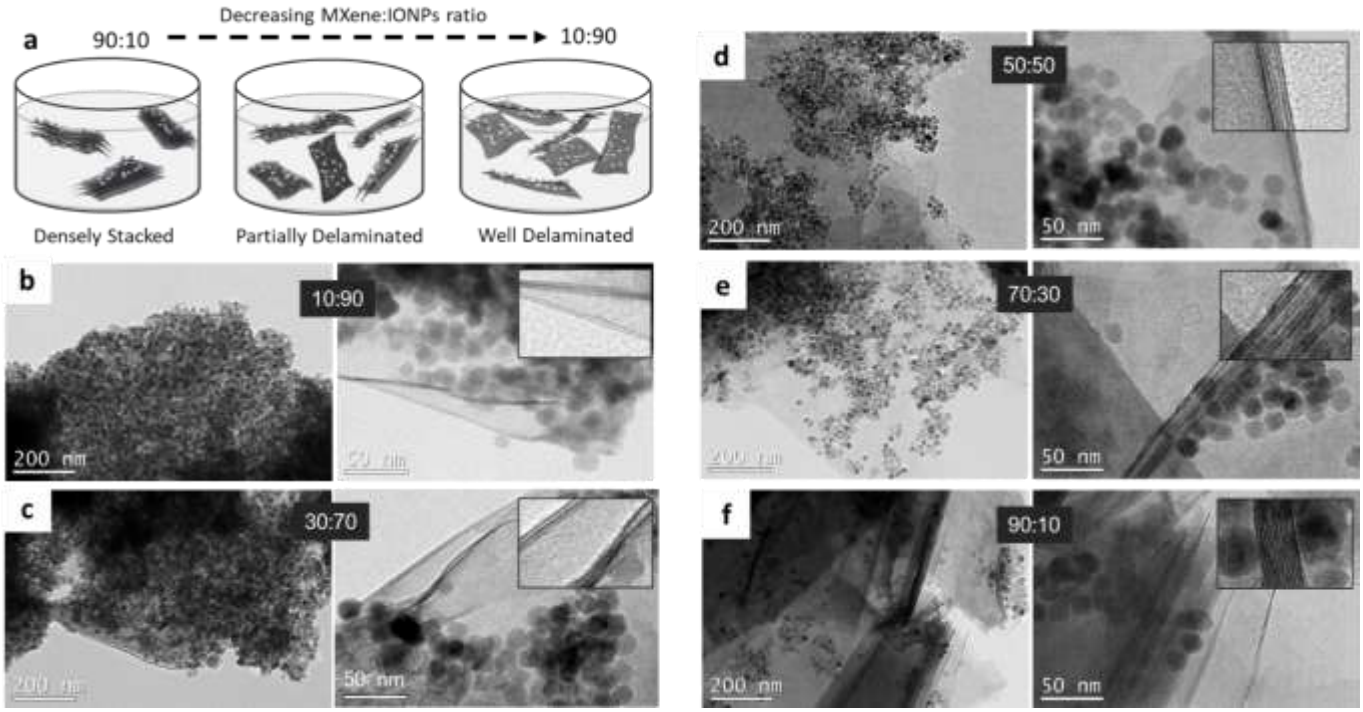

Fig. 5. (a) Schematic illustration of the relationship between the MNPs concentration and the final morphology of the $Ti_3C_2T_x/Fe_3O_4$ hybrids during the fabrication process in THF. At low concentrations of IONPs, stacks of MXene layers are formed. At high concentrations, delaminated hybrids are obtained. (b, c, d, e and f) TEM micrograph of

the 10:90, 30:70, 50:50, 70:30 and 90:10 mass ratio hybrids respectively captured at ×25000 (left) and ×100000 (right) magnification.

2.4. $Ti_3C_2T_x$/Fe_3O_4 nanohybrids photothermal behavior

MXenes are electrically conductive materials with efficient electromagnetic wave absorption across a broad spectrum. In particular, $Ti_3C_2T_x$-type MXenes are capable of absorbing electromagnetic radiation in the NIR I and II ranges [30], demonstrating highly efficient light-to-heat conversion. This superior absorption, particularly in the NIR-II range, underscores the potential for photothermal applications of delaminated MXenes. Aqueous suspensions of delaminated MXenes were prepared at concentrations from 0.01 to 0.1 mg/mL and their absorption was measured using UV-Vis spectroscopy allowing us to estimate a notable extinction coefficient of approximately 18.9 L g^{-1} cm^{-1} at λ = 1064 nm (**Fig. S3**). This value is consistent with previously reported data [30,65] supporting the conclusion that the MXene exhibits good light absorption properties, well above those of oxidized graphite nanosheets (GO) [66]. Absorptivities as high as ε = 52.8 L g^{-1} cm^{-1} at λ = 808 nm have been reported for MXene quantum dots (QD) [67]. The absorptivity of MXenes depends strongly on factors such as particle size, surface functional groups and interplanar spacing. Note that superior performance of MXene quantum dots (QD) is attributed to their significantly reduced size (4.9 nm), which enhances light absorption efficiency. However, the absorption properties of our dMXene clearly surpass those other 2D nanomaterials in the NIR II region emphasizing its exceptional potential. Compared to MXenes, dispersions of IONPs of the same concentration show lower absorption in the NIR region. This absorption is, in any case, not negligible. It is well known that magnetite exhibits a broad absorption band in the near-infrared region (around 1300–1700 cm^{-1}), which is attributed to an intervalence charge transfer (IVCT) transition between Fe^{2+} and Fe^{3+} ions in the octahedral sites of its inverse spinel structure [68]. The absorptivity of

each hybrid has been also measured and compared with the pure MXene and IONPs (**Fig. 6a**). Absorptivity at 1064 nm (laser wavelength) decreases as the amount of nanoparticles increases in the hybrid, although it is yet noticeable for the hybrids with the highest proportion of MXene. This behaviour has been also observed in other hybrids, such as MXene/PTFE [69] or MXene/CoFerrite [70]. Decreasing the amount of the MXene in the hybrid leads to reduced absorptivity.

Both the pure MXene and its hybrids were submitted to photothermal characterization, to assess their light-to-heat conversion efficiency. The evaluation was performed using a NIR laser (1064 nm) applied for 300 seconds at a power of 1 W power (P/A = 26 W/cm^2). The response of the materials was evaluated at a low concentration of 0.2 mg/mL (total mass) in water. **Fig. 6b** presents the heating curves of both the hybrid and pristine materials under irradiation. IONPs in aqueous suspension, in the absence of MXene sheets, led to minimal temperature increases of only 0.9 °C, within a 300 s irradiation period, indicating very limited and nearly negligible photothermal performance, primarily due to their low concentration in solution.

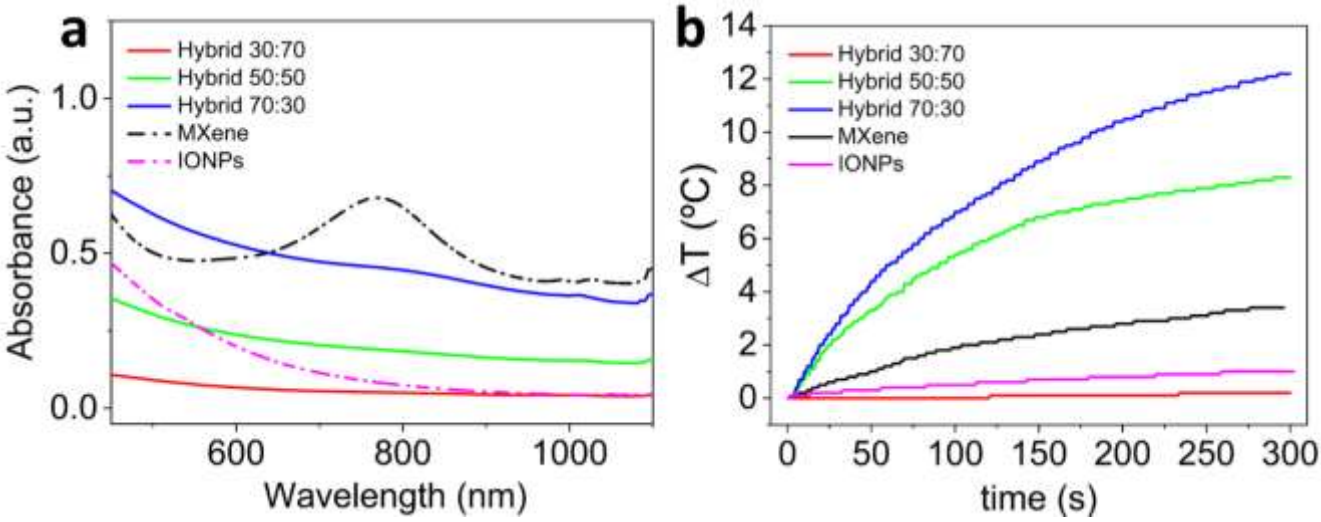

Fig. 6. (a) Vis-NIR absorption spectra of the hybrids and nanoparticles (b) Photothermal heating curves of hybrids and nanoparticles.

Fe_3O_4 nanoparticles have been widely studied as photothermal agents due to their semiconducting properties and the presence of a broad localized surface plasmon resonance (LSPR) band in the near-infrared (NIR) region [71]. This plasmonic behavior, particularly pronounced in non-stoichiometric compositions ($Fe_{3-x}O_4$), enables heat generation upon NIR irradiation [72]. However, the efficiency of this response is highly dependent on the excitation wavelength. The position and intensity of the LSPR band are influenced by factors such as morphology, size, crystalline imperfections, and agglomeration, among others [73]. Although the LSPR band of Fe_3O_4 extends over a broad spectral range, its maximum is typically located above 1300 nm. Therefore, under irradiation at 1064 nm, the photothermal response tends to be significantly lower, especially at low nanoparticle concentrations.

The irradiation of the synthesized MXene without IONPs results in a temperature increase of 3.4 °C. This is attributed to the located surface plasmon resonance (LSPR) possible in MXenes due to their semi-metallic character in the monolayer state and the high density of free charge carriers provided by surface T_x terminations, primarily –OH and $–F^-$) [8,45]. Additionally, MXene monolayers exhibit an intense absorption band around 800 nm, corresponding to an intra-band transition that facilitates efficient electromagnetic radiation [74]. Unlike Fe_3O_4 nanoparticles, which have a light-to-heat conversion efficiency ranging 2–90%, MXenes achieve nearly 100% efficiency [30]. This difference explains, in part, the lower photothermal response observed for Fe_3O_4 nanoparticles [64].

Analyzing the heating curves of the hybrids, compositions 70:30 and 50:50 reached remarkable temperature increments of 12.2, and 8.2 °C respectively. Notably, the photothermal response of the nanohybrids exceeds that of the individual base materials, demonstrating a clear synergic effect. However, the 30:70 hybrids exhibited negligible

photothermal capacity, which is correlated with the low absorptivity observed in this sample. This reduced absorptivity may be due to the formation of multilayered Fe_3O_4 nanoparticle clusters on the MXene surface, which can hinder light penetration and compromise the light absorption of the hybrid structure [75].

The heat generation capacity is commonly evaluated employing the specific absorbance rate (SAR), as defined in **Eq. (1)**. SAR considers the initial slope of the heating curve, (typically during the first 10 seconds), the specific heat of the medium, and the concentration of the photoactive material. Since MXene is the primary contributor to the overall heat generation, SAR was calculated both based on the total hybrid amount and specifically as a function of the MXene content. The results of the determined SAR values, and the temperature differences achieved are summarized in **Table 2**.

$$\mathrm{SAR} = \frac{C_p \cdot \rho}{[\text{Active material}]} \cdot \frac{dT}{dt} \qquad (1)$$

In this respect, C_p represents the specific heat of the measuring medium (solvent), ρ the density of the medium, divided by the concentration of the active material, and multiplied by the slope of the first 10 seconds of the heating curve (dT/dt).

Table 2. Final ΔT (ºC) values of the photothermal heating curves and the corresponding SAR values as a function of the MXene mass (W/g MXene) and the hybrids total mass (W/g hybrid).

Sample	[IONPs] (mg/mL)	[MXene](mg/mL)	ΔT^{o}_{final} (ºC)	SAR (W/g MXene)	SAR (W/g hybrid)
Hybrid 30:70	0.14	0.06	0.2	27.19	8.16
Hybrid 50:50	0.10	0.10	8.2	1153.45	576.72
Hybrid 70:30	0.06	0.14	12.2	1580.36	1106.26

MXene	–	0.20	3.4	241.74	241.74
IONPs	0.20	–	0.9	32.86	32.86

SAR of samples 50:50 and 70:30 (W/g of hybrid) are up to ≈2.4 and ≈4.6 times higher than the one of MXene alone. The exceptional behaviour exhibited by both hybrids may be caused by a conjunction of different factors. First, according to the SEM observations, both hybrids preserve the laminar structure of MXene sheets without apparent restacking. The main mechanism in light-to-heat energy conversion is LSPR, and this effect is strongly dependent on the geometrical parameters of the conducting nanoparticle. This effect was observed in metallic nanoparticles (*e.g.*, Au and Ag) and as well in MXenes. LSPR effect can be improved by decreasing thickness [76]. Therefore, multilayered MXenes (mlMXenes) exhibit lower performance in light-to-heat transfer compared to dMXenes. We surmise that a nanoparticle coating with sufficiently extensive coverage can effectively prevent MXene restacking and enhance light absorption and conversion compared to bare MXene sheets, provided that excessive loading—leading to clustered aggregates that hinder light interaction—is avoided. Representative TEM images of the nanohybrids were presented in **Fig. 5**. In addition to the varying degrees of coating observed in the SEM images, MXene sheets stackings ranging from 2–3 layers to massive stacks of up to 17 sheets can also be identified. The frequency of occurrence of these massive stacks is related to the MXene:Fe_3O_4 weight ratio. The higher the weight ratio is, the less frequently massive restacking appears. Another possible explanation for the synergy effect in PTT displayed by some of the hybrids can be found in the literature. It is associated with dual-plasmonic resonance, which occurs when two or more nanomaterials capable of giving the LSPR are combined.

By incorporating metallic nanostructures on a plasmonic semiconductor material (MXene), multiple plasmonic resonance modes are generated that may improve the

absorption and development of photothermal processes [32]. The LSPR band may change both in intensity and wavelength. However, controlling the positioning of these new LSPR bands is complex, since it depends on multiple factors, such as the surface state of the MXenes, the distribution of the nanoparticles on the surface, the degree of agglomerations, inter-particle distance, among others. When these dual-plasmonic systems are excited with discrete magnetic irradiation, variations in absorption band shifts due to different structural conditions can result in varying heating efficiencies [8]. Indeed, additional experimental work should be done to confirm this potential. SEM and TEM images revealed that when the proportion of IONPs exceeds 50%, the MXene structure becomes surrounded by multiple layers and clusters of magnetic nanoparticles, with noticeable aggregation. In contrast, nanohybrids with lower IONPs content maintain a visible MXene structure, with the nanoparticles evenly distributed on the surface. Moreover, dispersion stability in water of the 30:70 hybrids was compromised, with the subsequent aggregation during the experiment, suggesting that the laminar structure of MXene was lost in this hybrid.

The magneto-thermal characterization was performed at a constant frequency of 282 kHz at different magnetic fields: 9, 13 and 17 kA/m. **Fig. 7** shows the magnetic hyperthermia heating curves of $Ti_3C_2T_x/Fe_3O_4$ hybrid samples. SAR values were likewise determined according to **Eq. (1)** and are summarized in **Table 3**. We have selected the initial-slope method, which is the most applied method to determine *SAR* values. The analysis is based on the assumption that heat losses are negligible during a certain time interval at the beginning of the heating [77]. This method is simple to implement, and it is compatible with commercial magnetic hyperthermia AC applicators. SAR values are moderate overall, with the highest values observed for 50:50 hybrids (151 W/g Fe_3O_4). Nonetheless, these hybrids were able to induce a substantial temperature increase (up to

6 °C) in the diluted aqueous suspensions within 180 s of irradiation. This temperature increase was obtained using AMFs conditions that comply the existing limit of the $H \times f$ factor for cancer treatment by MHT in clinic ($\leq 5 \times 10^9$ A m^{-1} s^{-1}) established by Hergt *et al.* [78]. Given the superparamagnetic behaviour of our magnetic nanoparticles, as confirmed by VSM, the corresponding intrinsic loss power (ILP) values were also determined (see **Table 3**). ILP values standardize and universalize SAR measurements, facilitating comparisons by normalizing SAR values according to the applied alternating field H and the frequency f, as described in **Eq. (2)**. The hybrids display ILP values ranging from 1.25 to 2.08 nH m^2/kg, with the 50:50 hybrids showing the highest value. These values are lower than those obtained for the IONPs alone (2.52 nH m^2/kg).

$$\mathrm{ILP} = \frac{\mathrm{SAR}}{\mathrm{H}^2 \cdot \mathrm{f}} \qquad (2)$$

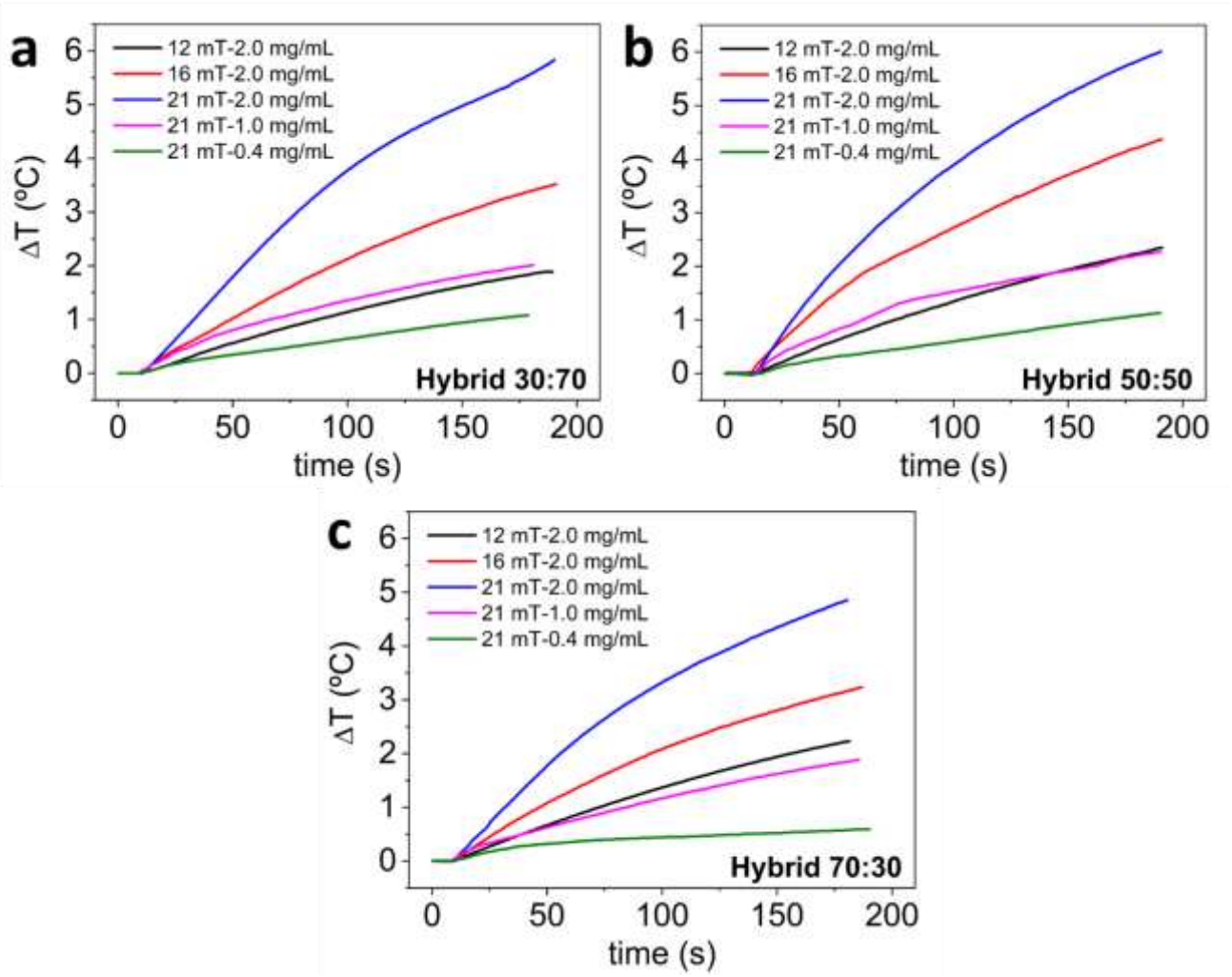

Fig. 7. Magnetic hyperthermia heating curves of $Ti_3C_2T_x/Fe_3O_4$ hybrid samples at different mass ratios: (a) 30:70, (b) 50:50 and (c) 70:30, at different fields (9, 13 and 17 kA/m) and different concentrations (2.0, 1.0 and 0.4 mg/mL) at a constant frequency of 282 kHz.

Table 3. Amounts of MXene and IONPs (in mg) used to prepare hybrids with different weight ratios, characterized at various concentrations under an alternating magnetic field (AMF) with a constant frequency (kHz) and different fields strengths (kA/m). The corresponding SAR values (W/g Fe_3O_4) and intrinsic loss power (ILP) were measured at a constant value frequency of 282 kHz.

	Hybrid (mg/mL)	**MXene (mg/mL)**	**IONPs (mg/mL)**	**Applied field (kA/m)**	**SAR (W/g Fe_3O_4)**	**ILP (nH m^2/kg)**
Hybrid 30:70	2.86	0.86	2.00	9	32	1.25
	2.86	0.86	2.00	12	67	1.47
	2.86	0.86	2.00	16	91	1.16
	1.43	0.43	1.00	16	98	1.25
	0.57	0.17	0.40	16	116	1.48
Hybrid 50:50	4.00	2.00	2.00	9	38	1.49
	4.00	2.00	2.00	12	95	2.08
	4.00	2.00	2.00	16	133	1.69
	2.00	1.00	1.00	16	144	1.83
	0.80	0.40	0.40	16	151	1.91
Hybrid 70:30	6.67	4.67	2.00	9	35	1.35
	6.67	4.67	2.00	12	61	1.33
	6.67	4.67	2.00	16	94	1.19
	6.67	2.33	1.00	16	100	1.28
	3.33	0.93	0.40	16	125	1.58
IONPs	–	–	2.00	9	31	1.19
	–	–	2.00	12	63	1.38
	–	–	2.00	16	126	1.60
	–	–	1.00	16	159	2.02
	–	–	0.40	16	199	2.52

SAR values are slightly higher (up to 199 W/g Fe_3O_4 for the same AMF conditions, heating curves are found in the supporting **Fig. S4**) than those of their corresponding hybrids, although likewise moderate. Indeed, it was reported that stabilizing of magnetic nanoparticles with oleic acid reduces SAR values and that oleic acid acts by entrapping the nanoparticles in such a way that the Brownian relaxation mechanisms [79] are reduced [80]. In addition, we assume that being IONPs on the surface MXene likewise contributes suppressing Brownian motion of the nanoparticles. As expected, the magnetothermal behaviour of the MXenes was negligible, as temperature was constant during AMF application.

Fig. 8 compiles the SAR values calculated from the magnetothermal results observed in **Fig. 7** (hybrids) or **Fig. S4** (IONPs) as a function of applied magnetic field (**Fig. 8a**) and Fe_3O_4 nanoparticles concentration (**Fig. 8b**). SAR increases with the magnetic field at a given frequency. Specifically, the free IONPs exhibit a quadratic evolution, consistent with the quadratic relationship between H_{max}^2 and the heat dissipation power [7]. In contrast, the hybrids show an evolution suggesting they are reaching saturation [81]. At high fields, the SAR value of the 50:50 hybrid is higher than that of all other samples, while the 30:70 and 70:30 hybrids exhibit lower responses, comparable to their corresponding free IONPs.

Fig. 8b shows the evolution of the SAR as a function of the IONPs concentration; in this sense, successive dilutions of all the samples studied were carried out experimentally. Specifically, samples were characterized at 2.0, 1.0 and 0.4 mg/mL of IONPs. In all cases, a significant decrease in SAR is observed at higher concentrations, suggesting that with increasing concentration there is a decrease in the interparticle distance, leading to an increase in the dipolar interaction, causing a decrease in SAR efficiency [82,83]. This phenomenon becomes more pronounced in free IONPs samples than in the nanohybrids,

as the nanoparticles in the hybrid are supported on MXenes and not freely arranged in the solution. In this context, nanohybrids with a 50:50 mass ratios exhibit higher performance than the rest, registering superior SAR values only at high concentrations. Studies on the dependence of SAR on concentration at various frequencies indicate that this relationship is influenced by multiple factors, including magnetic anisotropy, size, hydrodynamic volume, frequency, magnetic field, etc. [82]. While SAR values are expected to remain constant regardless of sample concentration [83], variations have been observed depending on factors such as nanoparticles coating, shape, size, anisotropy and measurement conditions, [84]. Overall, it can be concluded that the formation of 50:50 $Ti_3C_2T_x/Fe_3O_4$ hybrids does not compromise the heating performance of the incorporated IONPs.

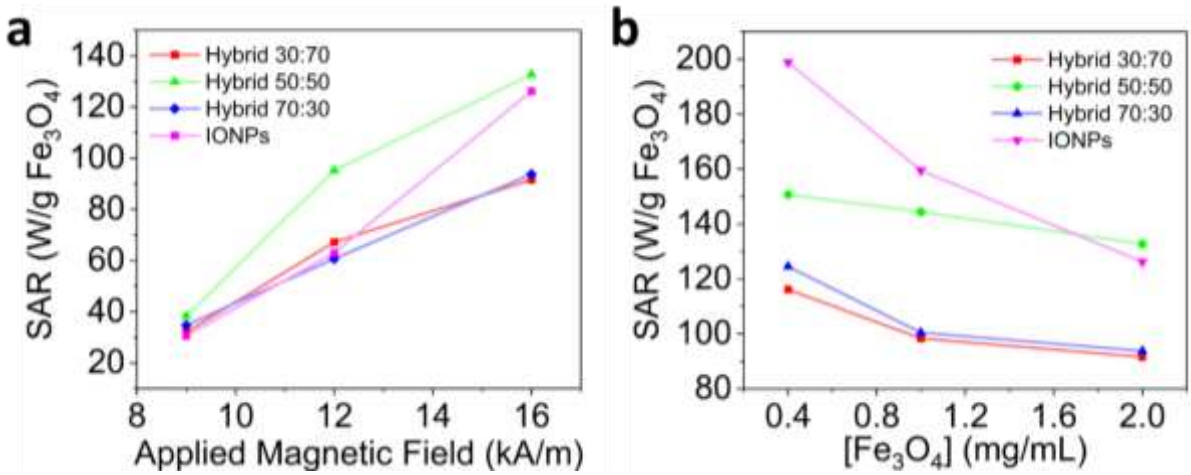

Fig. 8. SAR dependence on the (a) applied magnetic field and (b) Fe_3O_4 concentration of $Ti_3C_2T_x/Fe_3O_4$ nanohybrids of different mass ratios: 30:70, 50:50 and 70:30

3. Conclusion

Hybrid multifunctional nanomaterials based on delaminated $Ti_3C_2T_x$ MXenes and Fe_3O_4 magnetic nanoparticles were successfully prepared at different MXene:IONPs ratios (90:10, 70:30, 50:50, 30:70, 10:90) using a simple Van der Waals-facilitated self-assembly route. The combination of these two nanoparticles allowed the obtention of a material with both photothermal and magnetothermal responses, making them promising candidates for advanced hyperthermia therapies. Highly delaminated MXenes provide the hybrid with radiation absorption in the NIR II region and good light-to-heat conversion. The 14 nm Fe_3O_4 faceted nanoparticles used in this work are superparamagnetic and present a well-known magnetothermal effect under an alternating magnetic field (AMF). Significantly, the hybridization process did not compromise the magnetic nanoparticles' ability to interact with radiation or a magnetic field.

Furthermore, a significant synergist effect was observed in the photothermal behaviour of MXenes when decorated by IONPs, achieving SAR values of 1106 W/g for the 70:30 hybrid, 4.5 times higher than that of pure MXene. This enhancement is attributed to reduced restacking and improved absorption of delaminated MXene sheets. MXene/Fe_3O_4 hybrid nanomaterials demonstrated enhanced heat dissipation under both alternating magnetic field exposure and laser excitation. These findings highlight the potential of MXenes as an optimal platform for developing multifunctional hybrid materials tailored for complementary hyperthermia treatment therapies.

4. Experimental section

Synthesis of $Ti_3C_2T_x$-type MXene. $Ti_3C_2T_x$-type MXenes were obtained by a selective aluminum layer etching of the MAX phase Ti_3AlC_2 (–325 mesh, >99%, Nanografi) via in situ generation hydrofluoric acid (HF) method, following a modified procedure

designed by Gogotsi *et al.* [48]. In a typical synthesis, 30 mL of HCl (≥35%, Sigma-Aldrich) was added to a 10 mL deionized water solution containing LiF (99.98%, Across Organics BvBa) and Ti_2AlC_3 to obtain in situ HF. A 2:1 mass ratio of LiF:Ti_2AlC_3 was used (for example, in a typical experiment 8 g of LiF and 4 g of Ti_2AlC_3 were employed). Then, this solution is placed on a stirring hot plate and the etching reaction is allowed at 40 °C for 48 h under magnetic stirring. After etching, purification involved washing with deionized water until reaching a pH of 7, resulting in multilayered MXene, mlMXene delamination was achieved through vortexing for 48 h at 480 rpm to obtain delaminated MXenes (dMXene). To preserve dMXenes from oxidative processes, they were freeze-dried and stored under vacuum. The synthetic route is summarized in **Fig. 9**. The atomic arrangements of MAX phase and $Ti_3C_2T_x$-type MXene are illustrated in **Fig. S5**.

Synthesis of Fe_3O_4 NPs. Magnetic iron oxide nanoparticles (IONPs) varying the shape were prepared via thermal decomposition of iron(III) acetylacetonate ($Fe(acac)_3$) ensuring precise control over shape, size distribution, and reaction yield [85]. Briefly, IONPs were prepared by solving 20 mmol (4.61 g) of 1,2-tetradecanediol (TDD) (90%, Sigma-Aldrich), and 2 mmol (0.71 g) of $Fe(acac)_3$ (≥99%, Acros Organics BvBa) precursor in 36 mL of 1-octadecene (ODE) (90%, Sigma-Aldrich), and then mixing with 2 mL of oleylamine (OAm) (70%, Sigma-Aldrich), 4 mL of oleic acid (OA) (90%, Sigma-Aldrich) and 4 mL of benzaldehyde (BA) (≥99%, Sigma-Aldrich). To this end, a 100 mL 2-neck round bottom flask was used. All reagents were added in fixed molar amounts, and $Fe(acac)_3$ was added in the last place. The reaction was conducted under a continuous N_2 (g) flow (30 bubbles per min), preventing O_2 presence, and under magnetic stirring of 800 rpm. Using a heating mantle (labbox HM02-D heating blanket with stirring and Pt100 thermocouple), a temperature rise up to 110 °C was

followed by an isothermal stage, ensuring homogenization and oxygen displacement. The reaction was hold at this temperature for 30 min. Then, the N_2 flow was stopped, and temperature is increased to 280 °C (at a heating rate of 10 °C/min) for thermal decomposition of $Fe(acac)_3$ and under N_2 atmosphere using a balloon attached to the condenser. The total reaction time was 90 min. After cooling, the crude reaction was recovered with chloroform, and acetone was added as an anti-solvent. The purification step was done through centrifugation and subsequent redispersion in chloroform. Finally, Fe_3O_4 NPs coated with oleic acid were kept in chloroform. The synthetic route is summarized in **Fig. 9** and the outline of the evolution of IONPs is shown in more detail in **Fig. S6**.

Synthesis of $Ti_3C_2T_x/Fe_3O_4$ nanohybrids. The $Ti_3C_2T_x/Fe_3O_4$ nanohybrids were obtained following a holistic method based on ensuring the preferential interaction between both counterparts following the modified experimental procedure of the original one developed by Xu *et al*. [86]. In this sense, tetrahydrofuran (THF) (≥99.5%, Sigma-Aldrich) was chosen as the reaction medium because of its physicochemical properties that allow promoting van der Waals-facilitated self-assembly. Briefly, an appropriate amount of Fe_3O_4 nanoparticles to obtain 25 mg of hybrids were transferred from chloroform to the reaction medium, 300 mL of THF, by drying of the chloroform and subsequent re-dispersion in 10 mL of THF and then dilution to 300 mL in a beaker. After an exchange of the solvent from chloroform to tetrahydrofuran (THF) IONPs coated with oleic acid, were easily redispersed through sonication (Fisherbrand FB15051 ultrasonic bath, 37 kHz, 280 W). The samples were subjected to a continuous sonication at room temperature which ensured a totally homogeneous dispersion. Delaminated MXene films were redispersed in water to a final concentration of 2 mg/mL. Then, MXene dispersion was added to the IONPs dispersion drop by drop. After addition, sonication was

maintained for 5 h at room temperature. The nanohybrid dispersion was allowed to sediment overnight. The supernatant was discarded and the nanohybrids were vacuum dried. Varying the $Ti_3C_2T_x$:Fe_3O_4 mass ratio, different nanohybrids were synthetized:10:90, 30:70, 50:50, 70:30 and 90:10. The global experimental conditions are summarized in **Fig. 9**.

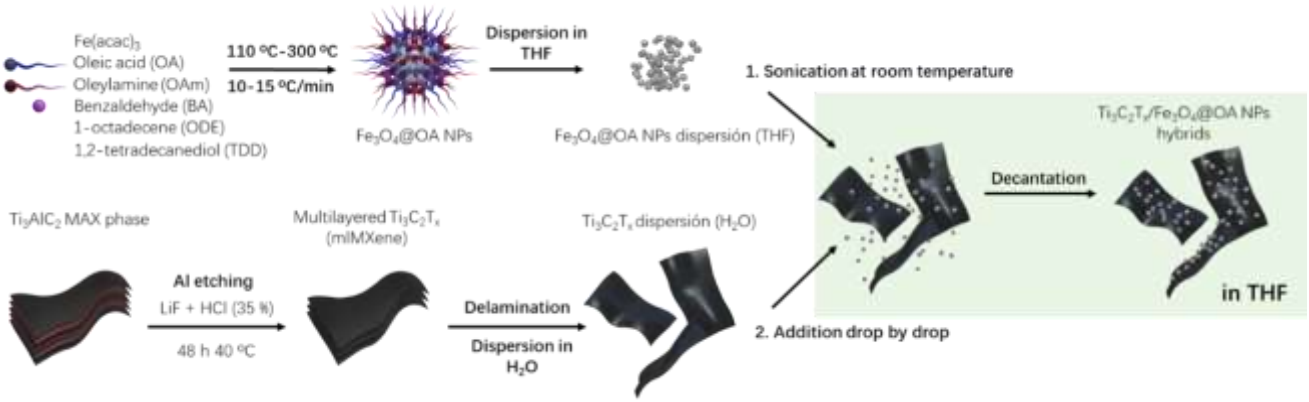

Fig. 9. Synthetic route of $Ti_3C_2T_x/Fe_3O_4$ hybrids in THF, starting from Fe_3O_4 NPs obtained following the thermal decomposition method of the $Fe(acac)_3$ precursor deposited on the delaminated $Ti_3C_2T_x$-type MXene films obtained following the selective etching of Al layers of the Ti_3AlC_2 MAX phase by in situ HF and subsequent delamination process.

Scanning Electron Microscopy (SEM) Characterization. Morphological studies of the dMXenes films and the different nanohybrids were carried out with FEI TENEO LoVAc Field Emission Scanning Electron Microscope (FE-SEM). Both dry materials were deposited on carbon tape.

Transmission Electron Microscopy (TEM) Characterization. The JEOL JEM 2100 HT Transmission Electron Microscope (TEM) allowed the structural evaluation of Fe_3O_4 NPs and $Ti_3C_2T_x/Fe_3O_4$ nanohybrids of different mass ratios; also, in the case of the IONPs it was possible to obtain size distributions after acquiring the intraparticle size with a population of 250 samples. The preparation of the samples was performed by depositing

a drop of a diluted solution of the nanoparticles in chloroform on a Cu with C holder, while the hybrids were dispersed in isopropanol and subsequently diluted in the same solvent and depositing a drop on the Cu with C holder and leaving them to dry at room temperature.

X-Ray Diffraction (XRD) Analysis. The crystallographic study was carried out with a Philips X'Pert-MPD equipment with Cu Kα radiation (λ = 0.15406 nm) with a scan rate of 0.2 2θ/min from 10 to 70° for the Fe_3O_4 NPs and from 4 to 70° for the dMXene films. Both materials were dispersed in acetone, deposited on the sample holder, and allowed to dry at room temperature.

X-ray Photoelectron Spectroscopy (XPS) characterization. X-ray photoelectron spectra were recorded with a multi- technique ultra-high vacuum system equipped with a SPECS PHOIBOS 100 MCD detector and non-monochromatic Mg Kα (*hv* = 1256.6 eV) X-ray radiation operating at 200 W (12 kV). The samples were degassed for 6–8 h, to achieve a dynamic vacuum below 10−8 Pa prior to analysis. The instrument's error in energy determinations was less than 0.01 eV. The resulting spectral data were analyzed using CASAXPS software (v2.3.26) and the RSF database by peak fitting after Shirley background correction.

Vibrating-Sample Magnetometer (VSM) Characterization. Magnetic properties were evaluated to Fe_3O_4 NPs with a KLA Tencor EV7 Vibrating-Sample Magnetometer (VSM) sweeping from a range of -5 to 5 (T) at a scanning speed of 0.3 T/min and at a constant temperature of 27 °C. Sample preparation consisted of depositing 100 μL of a dispersion of MNPS in CHCl3 on a cotton ball, which, after drying, was introduced into a pellet.

Dynamic Light Scattering (DLS) Characterization. The stability of the IONPs sample in the reaction medium for hybrid fabrication (THF) and with a Malvern Zetasizer Nano

ZS90 Dynamic Light Scattering (DLS) equipment the size distribution in terms of number and volume were recorded. The IONPs sample was dispersed in THF at a concentration of 1:40.

Atomic Emission Spectroscopy with Inductively Coupled Plasma (ICP-OES) Analysis. Using a SPECTRO Arcos ICP-OES spectrometer, an analytical study was carried out to determine the concentration of the IONP dispersion in terms of Fe. For the preparation, 50 μL of sample was digested in 4 mL of aqua regia for 24 h at 90 °C and the mixture was brought to 50 mL.

Visible Near-infrared (Vis-NIR) Absorption Analysis. Vis-NIR absorption was analyzed up to 1100 nm (NIR II) for aliquots of different dispersions in water, in the range of 0.01–0.10 mg/mL, of MXene nanosheets, IONPs and the different hybrids. Analysis was performed using a Zuzi 4260/50 spectrophotometer with a bandwidth of 1 nm.

Photothermia – Calorimetric. The nanohybrids 30:70, 50:50 and 70:30, dMXene, and IONPs were evaluated for their photothermal properties by exciting them with a Novanta Ventus HP MPC6000 laser (2.2 mm beam diameter) at λ = 1064 nm at 1 W (P/A = 26 W/cm^2) for 300 s. Hybrid samples were dispersed in water at a fixed concentration of 0.2 mg/mL, which 500 μL of this dispersion were placed in a 2 mm optical pitch quartz cuvette (under magnetic stirring), lasered for 300 s at 1 W power recording the temperature evolution with a T-type thermocouple coupled to a USB Datalogger (TC direct). The determination of the specific absorption rate (SAR) involved analyzing the slope (dT/dt) of the initial heating profile within the first 10 seconds. **Eq. (1)** was subsequently applied, taking into consideration the quantity of MXene and the total weight of the hybrid material.

Magnetic Hyperthermia – Calorimetric. The magnetic hyperthermia properties of 30:70, 50:50 and 70:30 hybrids, dMXenes and IONPs were studied employing a Fives

Celes 12118 M01 alternating magnetic field (AMF) generator at a frequency of 282 kHz, equipped with a 6-turn and a thermostatic bath set at 25 °C for the samples. Samples were adjusted to a concentration of 2 mg magnetic nanoparticles/mL H_2O. The heating profile was recorded using an Osensa FTX fiber optic temperature sensor. Measurements were performed at different field conditions (9, 13 and 17 kA/m) for 180 s. The specific absorption rate (SAR) was estimated by considering the slope (dT/dt) of the heating profile the first 10 s and using **Eq. (1)**, considering only the concentration of magnetic nanoparticles. The intrinsic loss power (ILP) parameter was also calculated applying **Eq. (2)**.

CRediT authorship contribution statement

Zhu Peng Shen: Investigation, Methodology, Data curation, Formal analysis, Writing – original draft. **Juan Carlos Cabanelas:** Investigation, Methodology, Formal analysis, Supervision, Writing – original draft. **Helena Gavilán and María B Serrano:** Conceptualization, Investigation, Methodology, Supervision, Writing – original draft, Writing – review & editing. **Álvaro Gallo-Cordova, Lucía Gutiérrez, Verónica S Miguel and Ángel Maroto-Valiente:** Investigation, Methodology, Formal analysis, Writing – review & editing**. Yílian Fernández-Afonso and Julio Marco Cuenca**: Investigation, Methodology, Writing – review & editing.

Declaration of competing interest

The authors declare no conflict of interest.

Data availability

Several datasets are presented in Supplementary data to this article. Additional data will be made available on request.

Funding

This work was supported by Grant PID2021-125302NB-I00 funded by Spanish MCIN/AEI/ 10.13039/501100011033 and, as appropriate, by "ERDF A way of making Europe"

H.G acknowledges the financial support from the Spanish Government through grant RYC2021-032448-I and A.G.-C acknowledges the financial support from the Spanish Government through grant No. TED2021-130191B-C43. This publication is based upon work from COST Action CA23132 (NexMPI), supported by COST (European Cooperation in Science and Technology). The funding for the publication of this paper was covered by Universidad Carlos III de Madrid.

Appendix A. Supplementary data

References

[1] X. Liu, Y. Zhang, Y. Wang, W. Zhu, G. Li, X. Ma, Y. Zhang, S. Chen, S. Tiwari, K. Shi, S. Zhang, H.M. Fan, Y.X. Zhao, X.J. Liang, Comprehensive understanding of magnetic hyperthermia for improving antitumor therapeutic efficacy, Theranostics 10 (2020) 3793–3815. https://doi.org/10.7150/thno.40805.

[2] H.S. Han, K.Y. Choi, Advances in nanomaterial-mediated photothermal cancer therapies: Toward clinical applications, Biomedicines 9 (2021). https://doi.org/10.3390/biomedicines9030305.

[3] D. Zhi, T. Yang, J. O'Hagan, S. Zhang, R.F. Donnelly, Photothermal therapy, Journal of Controlled Release 325 (2020) 52–71. https://doi.org/10.1016/j.jconrel.2020.06.032.

[4] E.C. Abenojar, S. Wickramasinghe, J. Bas-Concepcion, A.C.S. Samia, Structural effects on the magnetic hyperthermia properties of iron oxide nanoparticles, Progress in Natural Science: Materials International 26 (2016) 440–448. https://doi.org/10.1016/j.pnsc.2016.09.004.

[5] K.D. Bakoglidis, K. Simeonidis, D. Sakellari, G. Stefanou, M. Angelakeris, Size-dependent mechanisms in AC magnetic hyperthermia response of iron-oxide nanoparticles, IEEE Trans Magn 48 (2012) 1320–1323. https://doi.org/10.1109/TMAG.2011.2173474.

[6] S.K. Sharma, N. Shrivastava, F. Rossi, L.D. Tung, N.T.K. Thanh, Nanoparticles-based magnetic and photo induced hyperthermia for cancer treatment, Nano Today 29 (2019). https://doi.org/10.1016/j.nantod.2019.100795.

[7] H. Gavilán, S.K. Avugadda, T. Fernández-Cabada, N. Soni, M. Cassani, B.T. Mai, R. Chantrell, T. Pellegrino, Magnetic nanoparticles and clusters for magnetic hyperthermia: optimizing their heat performance and developing combinatorial therapies to tackle cancer, Chem. Soc. Rev. 50 (2021) 11614–11667. https://doi.org/10.1039/D1CS00427A.

[8] X. Cui, Q. Ruan, X. Zhuo, X. Xia, J. Hu, R. Fu, Y. Li, J. Wang, H. Xu, Photothermal Nanomaterials: A Powerful Light-to-Heat Converter, Chem Rev 123 (2023) 6891–6952. https://doi.org/10.1021/acs.chemrev.3c00159.

[9] R. Weissleder, A clearer vision for in vivo imaging, Nat Biotechnol 19 (2001) 316–317. https://doi.org/10.1038/86684.

[10] A.M. Smith, M.C. Mancini, S. Nie, Second window for in vivo imaging, Nat Nanotechnol 4 (2009) 710–711. https://doi.org/10.1038/nnano.2009.326.

[11] D. He, H. Li, Y. Li, Z. Xu, C. Wang, Y. Tang, F. Wu, X. Zhen, S. Wang, Tumor-targeting semiconducting polymer nanoparticles: efficient adjuvant photothermal therapy using ultra-low laser power inhibits recurrences after breast-conserving surgery, Nanoscale 15 (2023) 6252–6262. https://doi.org/10.1039/D2NR06692K.

[12] G. Hegyi, G.P. Szigeti, A. Szász, Hyperthermia versus oncothermia: Cellular effects in complementary cancer therapy, Evidence-Based Complementary and Alternative Medicine 2013 (2013). https://doi.org/10.1155/2013/672873.

[13] C. Moorthi, R. Manavalan, K. Kathiresan, Nanotherapeutics to Overcome Conventional Cancer Chemotherapy Limitations, 2011. www.cspsCanada.org.

[14] B. Mehdaoui, A. Meffre, J. Carrey, S. Lachaize, L.M. Lacroix, M. Gougeon, B. Chaudret, M. Respaud, Optimal size of nanoparticles for magnetic hyperthermia: A combined theoretical and experimental study, Adv Funct Mater 21 (2011) 4573–4581. https://doi.org/10.1002/adfm.201101243.

[15] M. Levy, A. Quarta, A. Espinosa, A. Figuerola, C. Wilhelm, M. García-Hernández, A. Genovese, A. Falqui, D. Alloyeau, R. Buonsanti, P.D. Cozzoli, M.A. García, F. Gazeau, T. Pellegrino, Correlating magneto-structural properties to hyperthermia performance of highly monodisperse iron oxide nanoparticles prepared by a seeded-growth route, Chemistry of Materials 23 (2011) 4170–4180. https://doi.org/10.1021/cm201078f.

[16] K. Mahmoudi, A. Bouras, D. Bozec, R. Ivkov, C. Hadjipanayis, Magnetic hyperthermia therapy for the treatment of glioblastoma: a review of the therapy's history, efficacy and application in humans, International Journal of Hyperthermia 34 (2018) 1316–1328. https://doi.org/10.1080/02656736.2018.1430867.

[17] M.R.K. Ali, Y. Wu, M.A. El-Sayed, Gold-Nanoparticle-Assisted Plasmonic Photothermal Therapy Advances Toward Clinical Application, Journal of Physical Chemistry C 123 (2019) 15375–15393. https://doi.org/10.1021/acs.jpcc.9b01961.

[18] Z. Li, H. Lei, A. Kan, H. Xie, W. Yu, Photothermal applications based on graphene and its derivatives: A state-of-the-art review, Energy 216 (2021). https://doi.org/10.1016/j.energy.2020.119262.

[19] F. Wu, Y. Lu, X. Mu, Z. Chen, S. Liu, X. Zhou, S. Liu, Z. Li, Intriguing H-Aggregates of Heptamethine Cyanine for Imaging-Guided Photothermal Cancer Therapy, ACS Appl Mater Interfaces 12 (2020) 32388–32396. https://doi.org/10.1021/acsami.0c07608.

[20] L. Gong, L. Yan, R. Zhou, J. Xie, W. Wu, Z. Gu, Two-dimensional transition metal dichalcogenide nanomaterials for combination cancer therapy, J Mater Chem B 5 (2017) 1873–1895. https://doi.org/10.1039/c7tb00195a.

[21] H. Chen, T. Liu, Z. Su, L. Shang, G. Wei, 2D transition metal dichalcogenide nanosheets for photo/thermo-based tumor imaging and therapy, Nanoscale Horiz 3 (2018) 74–89. https://doi.org/10.1039/c7nh00158d.

[22] W. Yin, L. Yan, J. Yu, G. Tian, L. Zhou, X. Zheng, X. Zhang, Y. Yong, J. Li, Z. Gu, Y. Zhao, High-throughput synthesis of single-layer MoS2 nanosheets as a near-infrared photothermal-triggered drug delivery for effective cancer therapy, ACS Nano 8 (2014) 6922–6933. https://doi.org/10.1021/nn501647j.

[23] X. Wang, Q. Chen, C. Shen, J. Dai, C. Zhu, J. Zhang, Z. Wang, Q. Song, L. Wang, H. Li, Q. Wang, Z. Liu, Z. Luo, X. Huang, W. Huang, Spatially Controlled Preparation of Layered Metallic-Semiconducting Metal Chalcogenide Heterostructures, ACS Nano 15 (2021) 12171–12179. https://doi.org/10.1021/acsnano.1c03688.

[24] A. Zhang, A. Li, W. Zhao, J. Liu, Recent Advances in Functional Polymer Decorated Two-Dimensional Transition-Metal Dichalcogenides Nanomaterials for Chemo-Photothermal Therapy, Chemistry - A European Journal 24 (2018) 4215–4227. https://doi.org/10.1002/chem.201704197.

[25] M. Kim, J.H. Lee, J.M. Nam, Plasmonic Photothermal Nanoparticles for Biomedical Applications, Advanced Science 6 (2019). https://doi.org/10.1002/advs.201900471.

[26] J. Chen, Z. Ye, F. Yang, Y. Yin, Plasmonic Nanostructures for Photothermal Conversion, Small Science 1 (2021). https://doi.org/10.1002/smsc.202000055.

[27] Z.H. Jaffari, M.B. Khan, D. Kumar, X. Zhang, C. Li, S.M. Lam, Recent progress in Ti3C2Tx-based materials: From fundamentals to emerging applications, Mater Sci Semicond Process 148 (2022). https://doi.org/10.1016/j.mssp.2022.106835.

[28] S. Golovynskyi, I. Golovynska, L.I. Stepanova, O.I. Datsenko, L. Liu, J. Qu, T.Y. Ohulchanskyy, Optical windows for head tissues in near-infrared and short-wave infrared regions: Approaching transcranial light applications, J Biophotonics 11 (2018). https://doi.org/10.1002/jbio.201800141.

[29] J. Cao, B. Zhu, K. Zheng, S. He, L. Meng, J. Song, H. Yang, Recent Progress in NIR-II Contrast Agent for Biological Imaging, Front Bioeng Biotechnol 7 (2020). https://doi.org/10.3389/fbioe.2019.00487.

[30] R. Li, L. Zhang, L. Shi, P. Wang, MXene Ti3C2: An Effective 2D Light-to-Heat Conversion Material, ACS Nano 11 (2017) 3752–3759. https://doi.org/10.1021/acsnano.6b08415.

[31] H. Lin, X. Wang, L. Yu, Y. Chen, J. Shi, Two-Dimensional Ultrathin MXene Ceramic Nanosheets for Photothermal Conversion, Nano Lett 17 (2017) 384–391. https://doi.org/10.1021/acs.nanolett.6b04339.

[32] J. Liang, H. Liu, J. Yu, L. Zhou, J. Zhu, Plasmon-enhanced solar vapor generation, Nanophotonics 8 (2019) 771–786. https://doi.org/10.1515/nanoph-2019-0039.

[33] X. Fan, Y. Ding, Y. Liu, J. Liang, Y. Chen, Plasmonic Ti3C2Tx MXene Enables Highly Efficient Photothermal Conversion for Healable and Transparent Wearable Device, ACS Nano 13 (2019) 8124–8134. https://doi.org/10.1021/acsnano.9b03161.

[34] L. Gao, H. Chen, A. V. Kuklin, S. Wageh, A.A. Al-Ghamdi, H. Ågren, H. Zhang, Optical Properties of Few-Layer Ti3CN MXene: From Experimental Observations to Theoretical Calculations, ACS Nano 16 (2022) 3059–3069. https://doi.org/10.1021/acsnano.1c10577.

[35] Y. Wang, Y. Xu, M. Hu, H. Ling, X. Zhu, MXenes: Focus on optical and electronic properties and corresponding applications, Nanophotonics 9 (2020) 1601–1620. https://doi.org/10.1515/nanoph-2019-0556.

[36] K. Hantanasirisakul, Y. Gogotsi, Electronic and Optical Properties of 2D Transition Metal Carbides and Nitrides (MXenes), Advanced Materials 30 (2018) 1–30. https://doi.org/10.1002/adma.201804779.

[37] S. Gul, S.B. Khan, I.U. Rehman, M.A. Khan, M.I. Khan, A Comprehensive Review of Magnetic Nanomaterials Modern Day Theranostics, Front Mater 6 (2019). https://doi.org/10.3389/fmats.2019.00179.

[38] B. Rezaei, P. Yari, S.M. Sanders, H. Wang, V.K. Chugh, S. Liang, S. Mostufa, K. Xu, J.P. Wang, J. Gómez-Pastora, K. Wu, Magnetic Nanoparticles: A Review on Synthesis, Characterization, Functionalization, and Biomedical Applications, Small 20 (2024). https://doi.org/10.1002/smll.202304848.

[39] H. Gavilán, S.K. Avugadda, T. Fernández-Cabada, N. Soni, M. Cassani, B.T. Mai, R. Chantrell, T. Pellegrino, Magnetic nanoparticles and clusters for magnetic hyperthermia: Optimizing their heat performance and developing combinatorial therapies to tackle cancer, Chem Soc Rev 50 (2021) 11614–11667. https://doi.org/10.1039/d1cs00427a.

[40] M. Alhabeb, K. Maleski, B. Anasori, P. Lelyukh, L. Clark, S. Sin, Y. Gogotsi, Guidelines for Synthesis and Processing of Two-Dimensional Titanium Carbide (Ti3C2Tx MXene), Chemistry of Materials 29 (2017) 7633–7644. https://doi.org/10.1021/acs.chemmater.7b02847.

[41] P. Zhang, N. Sun, R.A. Soomro, S. Yue, Q. Zhu, B. Xu, Interface-Engineered Fe3O4/MXene Heterostructures for Enhanced Lithium-Ion Storage, ACS Appl Energy Mater 4 (2021) 11844–11853. https://doi.org/10.1021/acsaem.1c02649.

[42] A.C.Y. Yuen, T.B.Y. Chen, B. Lin, W. Yang, I.I. Kabir, I.M. De Cachinho Cordeiro, A.E. Whitten, J. Mata, B. Yu, H.D. Lu, G.H. Yeoh, Study of structure morphology and layer thickness of Ti3C2 MXene with Small-Angle Neutron Scattering (SANS), Composites Part C: Open Access 5 (2021). https://doi.org/10.1016/j.jcomc.2021.100155.

[43] A. Chae, S. Doo, D. Kim, T.Y. Ko, T. Oh, S.J. Kim, D.Y. Koh, C.M. Koo, Tunable Ti3C2TxMXene-Derived TiO2Nanocrystals at Controlled pH and Temperature, Langmuir 38 (2022) 12657–12665. https://doi.org/10.1021/acs.langmuir.2c02110.

[44] G. Perini, A. Rosenkranz, G. Friggeri, D. Zambrano, E. Rosa, A. Augello, V. Palmieri, M. De Spirito, M. Papi, Advanced usage of Ti3C2Tx MXenes for photothermal therapy on different 3D breast cancer models, Biomedicine and Pharmacotherapy 153 (2022). https://doi.org/10.1016/j.biopha.2022.113496.

[45] H. Lin, X. Wang, L. Yu, Y. Chen, J. Shi, Two-Dimensional Ultrathin MXene Ceramic Nanosheets for Photothermal Conversion, Nano Lett 17 (2017) 384–391. https://doi.org/10.1021/acs.nanolett.6b04339.

[46] G.P. Lim, C.F. Soon, N.L. Ma, M. Morsin, N. Nayan, M.K. Ahmad, K.S. Tee, Cytotoxicity of MXene-based nanomaterials for biomedical applications: A mini review, Environ Res 201 (2021) 111592. https://doi.org/https://doi.org/10.1016/j.envres.2021.111592.

[47] L. Chen, Y. Cao, X. Zhang, X. Guo, P. Song, K. Chen, J. Lin, Anisotropic and high thermal conductivity of epoxy composites containing multilayer Ti3C2Tx MXene nanoflakes, J Mater Sci 55 (2020) 16533–16543. https://doi.org/10.1007/s10853-020-05177-2.

[48] M. Alhabeb, K. Maleski, B. Anasori, P. Lelyukh, L. Clark, S. Sin, Y. Gogotsi, Guidelines for Synthesis and Processing of Two-Dimensional Titanium Carbide (Ti3C2Tx MXene), Chemistry of Materials 29 (2017) 7633–7644. https://doi.org/10.1021/acs.chemmater.7b02847.

[49] M. Shekhirev, C.E. Shuck, A. Sarycheva, Y. Gogotsi, Characterization of MXenes at every step, from their precursors to single flakes and assembled films, Prog Mater Sci 120 (2021) 100757. https://doi.org/https://doi.org/10.1016/j.pmatsci.2020.100757.

[50] C.B. Cockreham, V.G. Goncharov, E. Hammond-Pereira, M.E. Reece, A.C. Strzelecki, W. Xu, S.R. Saunders, H. Xu, X. Guo, D. Wu, Energetic Stability and Interfacial Complexity of Ti3C2Tx MXenes Synthesized with HF/HCl and CoF2/HCl as Etching Agents, ACS Appl Mater Interfaces 14 (2022) 41542–41554. https://doi.org/10.1021/acsami.2c09669.

[51] X. Zhao, A. Vashisth, E. Prehn, W. Sun, S.A. Shah, T. Habib, Y. Chen, Z. Tan, J.L. Lutkenhaus, M. Radovic, M.J. Green, Antioxidants Unlock Shelf-Stable Ti3C2Tx (MXene) Nanosheet Dispersions, Matter 1 (2019) 513–526. https://doi.org/https://doi.org/10.1016/j.matt.2019.05.020.

[52] V. Natu, M. Benchakar, C. Canaff, A. Habrioux, S. Célérier, M.W. Barsoum, A critical analysis of the X-ray photoelectron spectra of Ti3C2Tz MXenes, Matter 4 (2021) 1224–1251. https://doi.org/10.1016/j.matt.2021.01.015.

[53] T. Schultz, N.C. Frey, K. Hantanasirisakul, S. Park, S.J. May, V.B. Shenoy, Y. Gogotsi, N. Koch, Surface Termination Dependent Work Function and Electronic Properties of Ti3C2Tx MXene, Chemistry of Materials 31 (2019) 6590–6597. https://doi.org/10.1021/acs.chemmater.9b00414.

[54] L. Qiao, Z. Fu, J. Li, J. Ghosen, M. Zeng, J. Stebbins, P.N. Prasad, M.T. Swihart, Standardizing Size- and Shape-Controlled Synthesis of Monodisperse Magnetite (Fe3O4) Nanocrystals by Identifying and Exploiting Effects of Organic Impurities, ACS Nano 11 (2017) 6370–6381. https://doi.org/10.1021/acsnano.7b02752.

[55] H. Gavilán, G.M.R. Rizzo, N. Silvestri, B.T. Mai, T. Pellegrino, Scale-up approach for the preparation of magnetic ferrite nanocubes and other shapes with benchmark performance for magnetic hyperthermia applications, Nat Protoc 18 (2023) 783–809. https://doi.org/10.1038/s41596-022-00779-3.

[56] Crystal Structure, in: The Iron Oxides, John Wiley & Sons, Ltd, 2003: pp. 9–38. https://doi.org/https://doi.org/10.1002/3527602097.ch2.

[57] M.H. Phan, J. Alonso, H. Khurshid, P. Lampen-Kelley, S. Chandra, K.S. Repa, Z. Nemati, R. Das, Ó. Iglesias, H. Srikanth, Exchange bias effects in iron oxide-based nanoparticle systems, Nanomaterials 6 (2016). https://doi.org/10.3390/nano6110221.

[58] G. Salazar-Alvarez, J. Qin, V. Šepelák, I. Bergmann, M. Vasilakaki, K.N. Trohidou, J.D. Ardisson, W.A.A. Macedo, M. Mikhaylova, M. Muhammed, M.D. Baró, J. Nogués, Cubic versus spherical magnetic nanoparticles: The role of surface anisotropy, J Am Chem Soc 130 (2008) 13234–13239. https://doi.org/10.1021/ja0768744.

[59] C. Toyos-Rodríguez, J. Calleja-García, L. Torres-Sánchez, A. López, A.M. Abu-Dief, A. Costa, L. Elbaile, R.D. Crespo, J.S. Garitaonandia, E. Lastra, J.A. García, F.J. García-Alonso, A Simple and Reliable Synthesis of Superparamagnetic Magnetite Nanoparticles by Thermal Decomposition of Fe(acac)3, J Nanomater 2019 (2019). https://doi.org/10.1155/2019/2464010.

[60] Y. Zhang, J. Luo, B. Feng, H. Xu, Y. Sun, X. Gu, X. Hu, M. Naushad, B. Gao, H. Ren, Delamination of multilayer Ti3C2Tx MXene alters its adsorpiton and reduction of heavy metals in water, Environmental Pollution 330 (2023). https://doi.org/10.1016/j.envpol.2023.121777.

[61] Z. Yang, Y. Chen, G. Chen, J. Wang, H. Li, Ultrathin Ti3C2Tx MXene sheets with high electrochemically active area anchored Pt boosting hydrogen evolution, Heliyon 9 (2023). https://doi.org/10.1016/j.heliyon.2023.e19197.

[62] A. Rozmysłowska-Wojciechowska, T. Wojciechowski, W. Ziemkowska, L. Chlubny, A. Olszyna, A.M. Jastrzębska, Surface interactions between 2D Ti 3 C 2 /Ti 2 C MXenes and lysozyme, Appl Surf Sci 473 (2019) 409–418. https://doi.org/10.1016/j.apsusc.2018.12.081.

[63] S. Zhou, K. Guan, Z. Wang, Q. Song, Z. Li, P. Xu, L. Deng, S. Xiang, H. Matsuyama, Confined and mediated intercalation of nanoparticles in graphene oxide membrane to fine-tune desalination performance, Chemical Engineering Journal 465 (2023) 143005. https://doi.org/https://doi.org/10.1016/j.cej.2023.143005.

[64] Q. Wang, Y. Zhang, T. Hu, C. Meng, Fe3O4 nanoparticles/polymer immobilized on silicate platelets for crude oil recovery, Microporous and Mesoporous Materials 278 (2019) 185–194. https://doi.org/https://doi.org/10.1016/j.micromeso.2018.11.033.

[65] J. Xuan, Z. Wang, Y. Chen, D. Liang, L. Cheng, X. Yang, Z. Liu, R. Ma, T. Sasaki, F. Geng, Organic-Base-Driven Intercalation and Delamination for the Production of Functionalized Titanium Carbide Nanosheets with Superior Photothermal Therapeutic Performance, Angewandte Chemie 128 (2016) 14789–14794. https://doi.org/10.1002/ange.201606643.

[66] Z. Huang, X. Cui, S. Li, J. Wei, P. Li, Y. Wang, C.S. Lee, Two-dimensional MXene-based materials for photothermal therapy, Nanophotonics 9 (2020) 2233–2249. https://doi.org/10.1515/nanoph-2019-0571.

[67] X. Yu, X. Cai, H. Cui, S.W. Lee, X.F. Yu, B. Liu, Fluorine-free preparation of titanium carbide MXene quantum dots with high near-infrared photothermal performances for cancer therapy, Nanoscale 9 (2017) 17859–17864. https://doi.org/10.1039/c7nr05997c.

[68] P. Kharey, A. Indoliya, R. Gupta, R. Poddar, D. Sharma, S. Gupta, Near-infrared active superparamagnetic iron oxide nanoparticles for magnetomotive optical coherence tomography imaging and magnetic hyperthermia therapeutic applications, J Magn Magn Mater 549 (2022) 169038. https://doi.org/https://doi.org/10.1016/j.jmmm.2022.169038.

[69] H. Deng, J. Liao, J. Piao, Y. Zhang, S. He, Q. Zhou, Y. Li, L. Zhang, Polytetrafluoroethylene-intercalated MXene membranes with good photothermal performance for enhanced laser ignition, J Appl Polym Sci 137 (2020) 49137. https://doi.org/https://doi.org/10.1002/app.49137.

[70] M. Rizwan, V.A.L. Roy, R. Abbasi, S. Irfan, W. Khalid, M. Atif, Z. Ali, Novel 2D MXene Cobalt Ferrite (CoF@Ti3C2) Composite: A Promising Photothermal Anticancer In Vitro Study, ACS Biomater Sci Eng 10 (2024) 2074–2087. https://doi.org/10.1021/acsbiomaterials.3c01328.

[71] A.G. Roca, J.F. Lopez-Barbera, A. Lafuente, F. Özel, E. Fantechi, J. Muro-Cruces, M. Hémadi, B. Sepulveda, J. Nogues, Iron oxide nanoparticles (Fe3O4, γ-Fe2O3 and FeO) as photothermal heat mediators in the first, second and third biological windows, Phys Rep 1043 (2023) 1–35. https://doi.org/10.1016/j.physrep.2023.10.003.

[72] E.A. Dolgopolova, D. Li, S.T. Hartman, J. Watt, C. Ríos, J. Hu, R. Kukkadapu, J. Casson, R. Bose, A. V Malko, A. V Blake, S. Ivanov, O. Roslyak, A. Piryatinski, H. Htoon, H.-T. Chen, G. Pilania, J.A. Hollingsworth, Strong Purcell enhancement at telecom wavelengths afforded by spinel Fe3O4 nanocrystals with size-tunable plasmonic properties, Nanoscale Horiz. 7 (2022) 267–275. https://doi.org/10.1039/D1NH00497B.

[73] P. Pallavicini, G. Chirico, A. Taglietti, Harvesting Light To Produce Heat: Photothermal Nanoparticles for Technological Applications and Biomedical Devices, Chemistry - A European Journal 27 (2021) 15361–15374. https://doi.org/10.1002/chem.202102123.

[74] N. Khatun, S. Dey, G.C. Behera, S.C. Roy, Ti3C2Tx MXene functionalization induced enhancement of photoelectrochemical performance of TiO2 nanotube arrays, Mater Chem Phys 278 (2022) 125651. https://doi.org/https://doi.org/10.1016/j.matchemphys.2021.125651.

[75] Y. Gao, Z. Tang, X. Chen, J. Yan, Y. Jiang, J. Xu, Z. Tao, L. Wang, Z. Liu, G. Wang, Magnetically accelerated thermal energy storage within Fe3O4-anchored MXene-based phase change materials, Aggregate 4 (2023). https://doi.org/10.1002/agt2.248.

[76] D. Wang, Y. Fang, W. Yu, L. Wang, H. Xie, Y. Yue, Significant solar energy absorption of MXene Ti3C2Tx nanofluids via localized surface plasmon resonance, Solar Energy Materials and Solar Cells 220 (2021). https://doi.org/10.1016/j.solmat.2020.110850.

[77] I. Andreu, E. Natividad, Accuracy of available methods for quantifying the heat power generation of nanoparticles for magnetic hyperthermia, International Journal of Hyperthermia 29 (2013) 739–751. https://doi.org/10.3109/02656736.2013.826825.

[78] D. Kouzoudis, G. Samourgkanidis, A. Kolokithas-Ntoukas, G. Zoppellaro, K. Spiliotopoulos, Magnetic Hyperthermia in the 400–1,100 kHz Frequency Range Using MIONs of Condensed Colloidal Nanocrystal Clusters, Front Mater 8 (2021). https://doi.org/10.3389/fmats.2021.638019.

[79] Q.A. Pankhurst, J. Connolly, S.K. Jones, J. Dobson, Applications of magnetic nanoparticles in biomedicine, 2003.

[80] P.I.P. Soares, C.A.T. Laia, A. Carvalho, L.C.J. Pereira, J.T. Coutinho, I.M.M. Ferreira, C.M.M. Novo, J.P. Borges, Iron oxide nanoparticles stabilized with a bilayer of oleic

acid for magnetic hyperthermia and MRI applications, Appl Surf Sci 383 (2016) 240–247. https://doi.org/10.1016/j.apsusc.2016.04.181.

[81] M.A.A. Kerroum, C. Iacovita, W. Baaziz, D. Ihiawakrim, G. Rogez, M. Benaissa, C.M. Lucaciu, O. Ersen, Quantitative analysis of the specific absorption rate dependence on the magnetic field strength in znxfe3−xo4 nanoparticles, Int J Mol Sci 21 (2020) 1–24. https://doi.org/10.3390/ijms21207775.

[82] V. Narayanaswamy, S. Sambasivam, A. Saj, S. Alaabed, B. Issa, I.A. Al-Omari, I.M. Obaidat, Role of magnetite nanoparticles size and concentration on hyperthermia under various field frequencies and strengths, Molecules 26 (2021). https://doi.org/10.3390/molecules26040796.

[83] P. De La Presa, Y. Luengo, M. Multigner, R. Costo, M.P. Morales, G. Rivero, A. Hernando, Study of heating efficiency as a function of concentration, size, and applied field in γ-Fe2O3 nanoparticles, Journal of Physical Chemistry C 116 (2012) 25602–25610. https://doi.org/10.1021/jp310771p.

[84] A.E. Deatsch, B.A. Evans, Heating efficiency in magnetic nanoparticle hyperthermia, J Magn Magn Mater 354 (2014) 163–172. https://doi.org/https://doi.org/10.1016/j.jmmm.2013.11.006.

[85] O.S. Sánchez, T. Castelo-Grande, P.A. Augusto, J.M. Compaña, D. Barbosa, Cubic nanoparticles for magnetic hyperthermia: Process optimization and potential industrial implementation, Nanomaterials 11 (2021). https://doi.org/10.3390/nano11071652.

[86] P. Zhang, N. Sun, R.A. Soomro, S. Yue, Q. Zhu, B. Xu, Interface-Engineered Fe3O4/MXene Heterostructures for Enhanced Lithium-Ion Storage, ACS Appl Energy Mater 4 (2021) 11844–11853. https://doi.org/10.1021/acsaem.1c02649.